

ELPH

Annual Report 2021

Research Center for Electron Photon Science
Tohoku University

Preface

We are pleased to issue the Annual Report of 2021 for the Research Center for Electron-Photon Science (ELPH). This presents scientific and technical activities for the fiscal year 2021, in addition to the facility management status of ELPH, Tohoku University. We hope you will find this useful, together with another booklet published separately, which showcases the self-assessments of the faculty members of ELPH.

The fiscal year 2021 was my first year as the director of ELPH. I have started several new attempts to produce and sustain stable facility management. The first was to appoint a deputy director, and as of October 1st, Professor H. Onishi assumed this position. I have also prepared a new discretionary budget and solicited proposals from the facility members that would contribute to the stable operation of the facility, and further enhance research and educational activities. This was quite successful as there were multiple excellent proposals, especially from our younger staff members.

The fiscal year 2021 was also marked by a fortunate event that the base electricity rates were significantly lowered through competitive bidding (however, for the fiscal year 2022, all of this was completely wiped out by the Russian military invasion of Ukraine). In addition, the successful acquisition of competitive budgets, such as Grant-in-Aid for Scientific Research, provided a greater amount of indirect expenses. These contributed to the stable management of this research center and to securing budgetary flexibility, such as the aforementioned discretionary budgets.

At present, I am negotiating with the University Headquarters and the Ministry of Education, Culture, Sports, Science and Technology (MEXT) on a request for rather large size budgets of the renewal of accelerator-related equipment that needs to be replaced immediately, plus for the renovation of the 50-year-old accelerator building. This aims at ensuring the stable operation of the facility and enabling further cutting-edge research in the future.

I hope that you all understand and support these efforts, and we would appreciate the continued support from all users of our facility and related scientific communities.

November, 2022

Director

Toshimi Suda

ELPH Annual Report 2021

Contents

I. Papers

- Mass production of Sc-47 for cancer therapy by beta particles 1
A. Toyoshima, H. Kikunaga, Y. Shirakami, and H. Ikeda
- Performance evaluation of electron-multiplier tubes using a high-intensity electron beam for the T2K muon monitor 5
T. Honjo, T. Yamamoto, H. Nakamura, K. Takifuji, S. Kasama, K. Yasutome, A.K. Ichikawa, K.D. Nakamura, T. Kikawa, M. Ishitsuka, and T. Matsubara
- Production of Carrier Free Lu-177 by Photonuclear Reaction 13
K. Akiyama, A. Tamura, H. Kikunaga, and S. Kubuki
- Radiation tolerance tests with electron beam for Belle II silicon strip vertex detector 17
Y. Sato, F. Otani, K. Hara, T. Higuchi, A. Ishikawa, K. Nakamura, Y. Onuki, T. Shimasaki, H. Sudo, H. Tanigawa, T. Tsuboyama, Y. Uematsu, and Z. Wang
- The status report of LEPS2-solenoid experiment in 2021 19
Atsushi Tokiyasu and LEPS2 collaboration
- Improvement of a Mo/Si multi-layer mirror for the high-energy γ beam production by X-ray Compton scattering 25
N. Muramatsu, S. Datè, T. Harada, K. Kanda, M. Miyabe, S. Miyamoto, H. Ohkuma, M. Okabe, H. Shimizu, S. Suzuki, A. Tokiyasu, and T. Watanabe
- Performance evaluation of the Intermediate Tracker for sPHENIX 29
G. Nukazuka, C.W. Shih, Y. Sugiyama, Y. Akiba, H. En'yo, T. Hachiya, S. Hasegawa, M. Hata, H. Imai, M. Morita, I. Nakagawa, Y. Nakamura, G. Nakano, Y. Namimoto, R. Nouicer, M. Shibata, M. Shimomura, R. Takahama, K. Toho, M. Tsuruta, and M. Watanabe.

Development of aerogel Cherenkov detectors for use in the EMPHATIC hadron production experiment	39
M. Tabata, K. Okuhata, A. Kobayashi, T. Yuzawa, and H. Kawai	
Commissioning of the twin spectrometers for the ULQ ² experiment	43
C. Legris, T. Goke, Y. Honda, Y. Ishikura, M. Kohl, Y. Maeda, S. Miura, T. Muto, T. Suda, K. Tsukada, and H. Wauke	
Mass production of Sc-47 by photonuclear reaction for nuclear medicine application	57
H. Kikunaga, A. Toyoshima, H. Ikeda, and Y. Honda	

II . Status Report

III. List of Publication

IV. Members of Committees

V. Approved Experiments

I. Papers

(ELPH Experiment : #2987, #2998)

Mass production of Sc-47 for cancer therapy by beta particles

Atsushi Toyoshima¹, Hidetoshi Kikunaga², Yoshifumi Shirakami¹, and Hayato Ikeda²

¹Institute for Radiation Sciences, Osaka University, Toyonaka, 560-0043

²Research Center for Electron Photon Science (ELPH), Tohoku University, Sendai, 982-0826

Recently, we started studying mass-production and chemical purification of a new, accelerator-producible, medical radioisotope ^{47}Sc for the future medical application. We report our present status of the developments of large-scale production tests and purification procedures.

§1. Introduction

Targeted radionuclide therapy (TRT) is the cancer therapy in which administrated radionuclide-labelled pharmaceuticals are spontaneously accumulated in targeted tumors followed by internal irradiation of charged particles emitted from the radionuclide. At present, a few of TRT using ^{131}I , ^{90}Y , ^{177}Lu , and ^{223}Ra have been approved and utilized in Japan [1]. Recently, ^{177}Lu that emits β^- particles with a low average energy of 134 MeV and has a short half-life ($T_{1/2}$) of 6.65 d has been attracting worldwide attention. Medically used, carrier-free ^{177}Lu is produced from ^{176}Yb target by its neutron capture reaction and the β^- decay of produced ^{177}Yb using a nuclear reactor. However, it is not easy to produce and supply a mass amount of ^{177}Lu using a reactor in Japan. Therefore, we focused on accelerator-producible ^{47}Sc with low average energies of β^- particles (159 keV) and short half-life (3.35 d). Decay schemes of ^{47}Sc and ^{177}Lu [2] are shown in Fig. 1 and decay properties of them [3] are listed in Table 1. These properties of ^{47}Sc are similar to those of ^{177}Lu . In this study, we carried out mass production of ^{47}Sc via $^{nat}\text{Ti}(\gamma, p)^{47}\text{Sc}$ using the 70 MeV Linac accelerator and its chemical purification from the Ti target.

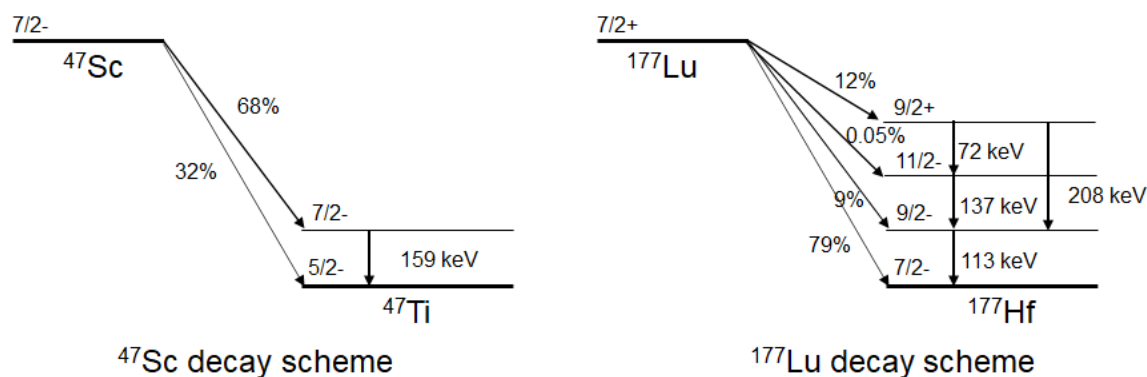


Fig. 1. Decay schemes of ^{47}Sc and ^{177}Lu [2].

Table 1. Decay properties of ^{47}Sc and ^{177}Lu [2].

Radionuclide	$T_{1/2}$ (day)	Average Beta energy (keV)	Gamma energy (keV) and intensity
^{47}Sc	3.35	162	159, 68%
^{177}Lu	6.65	134	113, 6%; 208 10%

§2. Experiments and preliminary results

^{47}Sc was produced in the $^{\text{nat}}\text{Ti}(\gamma, p)^{47}\text{Sc}$ reaction at the ELPH accelerator. Several grams of a TiO_2 target was enclosed in a quartz tube (Fig. 2a) and was irradiated by high-energy photon produced from a 30-MeV electron beam using the irradiation setup installed in shown in Fig. 2b. After a few hours of irradiation, the target was heated overnight in the chemistry laboratory. After dissolved, produced ^{47}Sc was chemically separated from the TiO_2 target using cation-exchange columns. This separation procedure was modified step-by-step. Chemical yields were approximately 80%. The separation was completed in a few days. In the near future, we will start performing a labelling by purified ^{47}Sc to a few typical substrates used for cancer therapy.

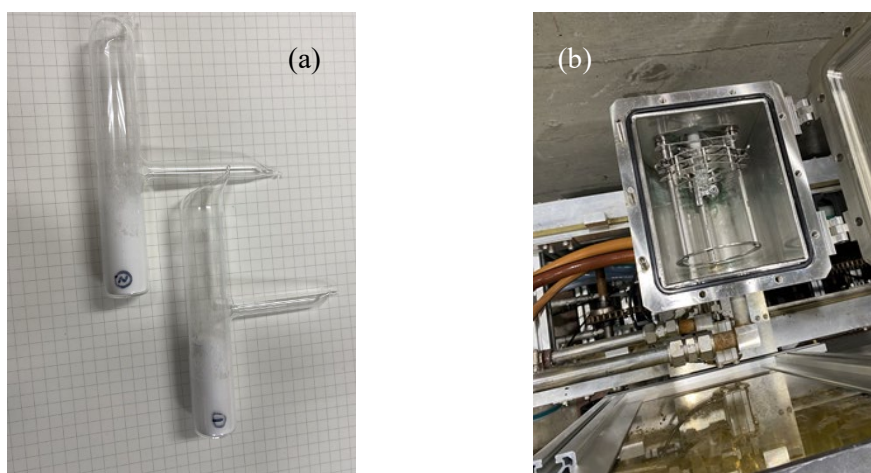


Fig. 2. (a) TiO_2 targets enclosed in quartz tubes and (b) irradiation chamber.

Acknowledgement

We express our gratitude to all the staff of ELPH for their invaluable assistance during the course of the experiments.

References

- [1] S. KINUYA: Nucl. Med. Mole. Imaging, **53** (2019) 35.

- [2] R. B. FIRESTONE: Table of Isotopes, 8th Ed. (1998).
[3] K. SIWOWSKA *et al.*: Pharmaceutics, **11** (2019) 424.

(ELPH Experiment : #2977)

Performance evaluation of electron-multiplier tubes using a high-intensity electron beam for the T2K muon monitor

T. Honjo¹, T. Yamamoto¹, H. Nakamura², K. Takifuji³, S. Kasama³,
K. Yasutome⁴, A.K. Ichikawa³, K.D. Nakamura³, T. Kikawa⁴, M. Ishitsuka²,
and T. Matsubara⁵

¹*Department of Physics, Osaka Metropolitan University, Osaka, 558-8585*

²*Department of Physics, Tokyo University of Science, Noda, Chiba, 278-8510*

³*Department of Physics, Tohoku University, Sendai, 980-8578*

⁴*Department of Physics, Kyoto University, Kyoto, 606-8502*

⁵*Institute of Particle and Nuclear Studies, High Energy Accelerator Research Organization(KEK), Tsukuba, 305-0801*

The electron-multiplier tube (EMT) is a candidate device of the muon monitor for the future high-intensity beam operation in the T2K experiment. Linearity and radiation tolerance the EMT have been already evaluated using a high-intensity 90 MeV electron beam from the injector LINAC at ELPH, Tohoku University in 2019-2020. In 2021, we performed electron beam test again. This time, we investigated initial unstable behaviour, the limit of the radiation tolerance and investigated the cause of radiation deterioration.

§1. Introduction

The T2K experiment is a long-baseline neutrino oscillation experiment to measure the neutrino oscillation parameters [1]. An intense (anti-)neutrino beam is produced at J-PARC (Japan Proton Accelerator Research Complex) and measured by the far detector, Super-Kamiokande, which is located 295 km away from J-PARC. The beam protons from the J-PARC accelerator impinge a graphite target, and charged pions are produced. Those pions decay in flight into pairs of a muon and a muon (anti-)neutrino.

The muon monitor is placed at 118 m from the target and measures the profile and intensity of the muon beam to indirectly monitor the neutrino production in real time [2]. The current muon monitor consists of 7×7 arrays of Si PIN photodiodes and ionization chambers. They have shown an excellent performance since the beginning of the T2K experiment [3]. The J-PARC main ring beam power as of 2021 is 510 kW. It will be increased up to 1.3 MW in the future [4, 5]. The Si PIN photodiodes and ionization chambers will not be applicable for the future high-intensity operation because of their issues of radiation tolerance and linearity, respectively.

As a candidate for a new muon monitor device, we have proposed and studied the electron-multiplier tube (EMT), which is equivalent to a photomultiplier tube without a photocathode. The EMTs were installed in the J-PARC muon monitor pit in 2017 and showed a good response to the muon beam [6].

We also conducted ELPH beam tests in 2019 (#2915) and 2020 (#2943), and confirmed that the EMT

linearity is sufficient and the radiation tolerance is much better than that of Si [7, 8]. However, initial instability, in which the gain decreases over several minutes after voltage application, has been observed in beam tests at J-PARC and ELPH. Therefore, the 3rd ELPH beam test was conducted in 2021 (#3007) to clarify the cause of initial instability, investigate the limits of radiation resistance, and investigate the causes of radiation deterioration [9, 10].

§2. Experimental Setup

We used a 90 MeV electron beam from the injector LINAC at ELPH. Figure 1 shows the experimental setup of the beam test. The detectors prepared this time are summarized in Table 1 together with their purposes. The CT and OTR are settled on the most upstream of the beam. The EMT, Si sensors, and Si array were attached on electric linear actuators so that they can be moved on and off the beam by remote control. Signals from the detectors except for the OTR were recorded by waveform digitizers (CAEN DT5725 and DT5740), after amplification or attenuation in some cases. OTR image was taken

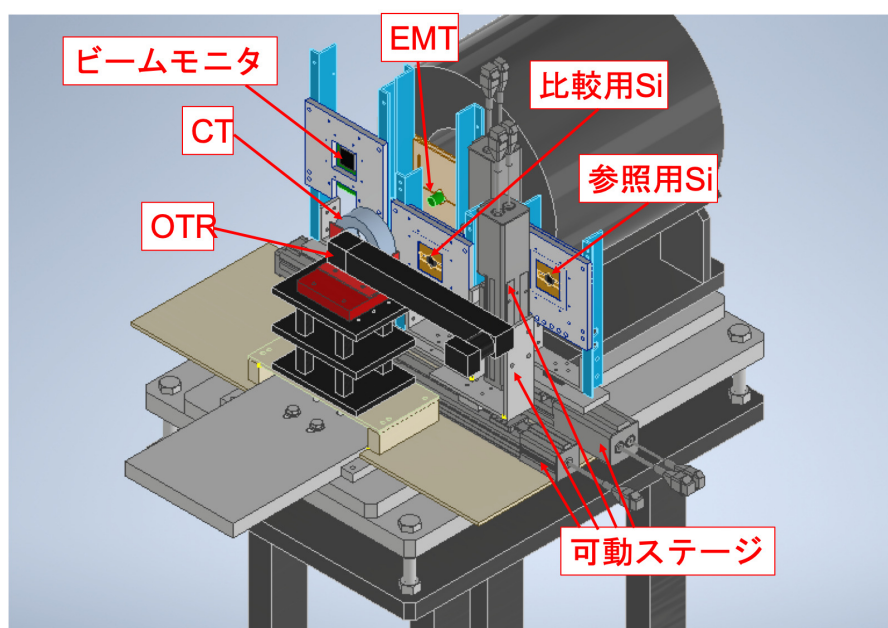


Fig.1. Experimental setup for 3rd ELPH beam test.

Table 1. The list of the detectors used in the 3rd ELPH beam test.

detector	Model number	purpose
EMT (electron multiplier tube)	R9880U (Hamamatsu)	performance evaluation target
Si (Si PIN photo diode)	53590-08 (Hamamatsu)	reference of EMT for low intensity beam
Si-array (64 channel Si array)	S13620-02 (Hamamatsu)	beam profile monitor for low intensity beam
CT (current transformer)	handmade	beam current monitor for high intensity beam
OTR (optical transition radiation monitor)	handmade	beam profile monitor for high intensity beam

by the dedicated camera. This detector arrangement was optimized by FLUKA simulations to minimize the effect of the multiple scattering.

There were three settings of the beam intensity, which roughly correspond to 1 pC/pulse (low intensity), 300 pC/pulse (medium intensity), and 20 nC/pulse (high intensity). Since the 1 pC/pulse is comparable to the J-PARC muon beam intensity, the detector response including linearity was evaluated in this setting. In the 300 pC/pulse and 20 nC/pulse settings, a large amount of the electron beam irradiated the detectors in a short time for studies of the initial stability and radiation tolerance. During high intensity beam irradiation, a 1Ω resistor was connected in parallel between the EMT signal and ground to prevent voltage drop due to excessive anode current.

From the beam profile measurement by the Si array, the beam width was measured to be $\sigma = 1.5$ mm, which is much smaller than the detector size (~ 10 mm). In order to irradiate the detector uniformly, the EMT were moved horizontally and vertically by the actuators during the beam exposure with middle/high intensity beam. Figure 2 shows the relative efficiency of high intensity beam irradiation by OTR monitor.

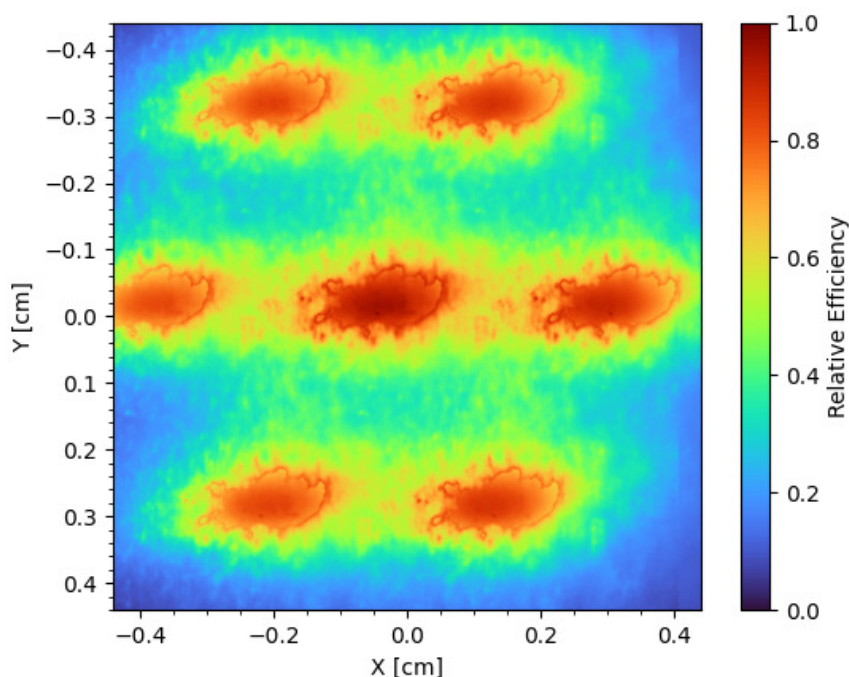


Fig.2. The estimated beam profile of high intensity beam. The beam profile measured by OTR are overlaid at 7 points with the EMT moved. The high intensity beam profile was found to be different from the low intensity one.

§3. Results

3.1 Initial stability

As an evaluation of the initial stability, a medium intensity beam was applied to the EMT, while a low intensity beam was applied to the EMT and Si to obtain the EMT signal for Si, and the dose dependence of the EMT signal was measured. Figure 3 shows the irradiation dose dependence of the EMT signal yield. The phenomenon that the signal decreased by several percent in the early stage, which was seen in J-PARC and 2nd ELPH beam test, was not observed. A possible reason for the initial instability is temperature change around the EMT. We measured the temperature dependence of the signal when the EMT was irradiated with light in the laboratory, and found that it had a temperature dependence of about $0.2\%/^{\circ}\text{C}$. In the future, it is necessary to measure the temperature dependence of the EMT signal from charged particles and to measure the temperature at the J-PARC site in detail.

3.2 Radiation tolerance

As an evaluation of the radiation tolerance, we performed similar procedure to the initial stability measurement except for the beam power. In this measurement, the high intensity beam was used instead of medium intensity one. Figure 4 shows the irradiation dose dependence of the EMT signal yield. It was found that radiation tolerance is maintained for 100 days even at 1.3 MW when signal degradation is required to be within 3%. In addition, even after a signal drop of about 10%, the decline seems to be stopped, and if the yield is well calibrated, it may be possible to continue using it for several years. We

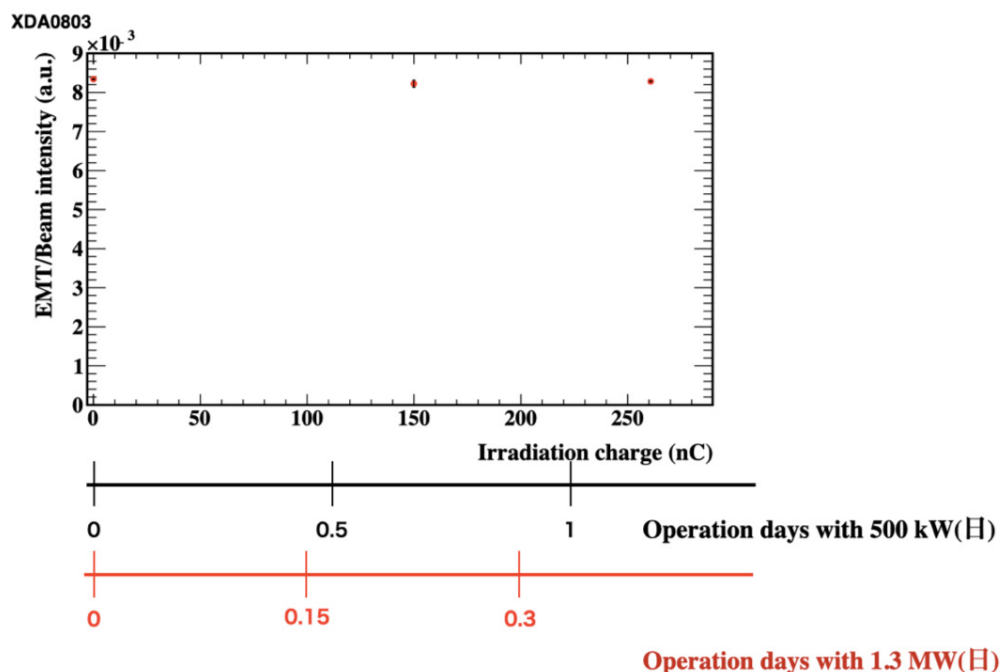


Fig.3. The irradiation charge dependence of the signal yield of the EMT. Additional horizontal axes are converted ones to the operation days of T2K experiment assuming current and future beam powers. The vertical axis is normalized by beam intensity measured by Si sensor.

also tested another EMT with high voltage (HV) off in order to check the too much amplification makes deterioration or not. Since the same deterioration was observed when the HV was turned off as when it was turned on, it was found that the main cause of the observed radiation deterioration was not the excessive electronic amplification of the EMT.

3.3 Radiation deterioration source investigation

In order to discriminate the cause of radiation deterioration, the EMT main body and the bleeder circuit were individually irradiated with electron beam. Figure 5 shows the signal yield changes for irradiating electron beam to the each components. For checking the EMT body, about 15% of signal decrease was observed. On the other hand, for the bleeder circuit case, about 10% of signal increase was observed. We measured the resistance and capacitance of the bleeder circuit after the beam test, and found no abnormal values compared to the specifications. Next time, it will be necessary to improve the accuracy and measure difference before and after beam irradiation.

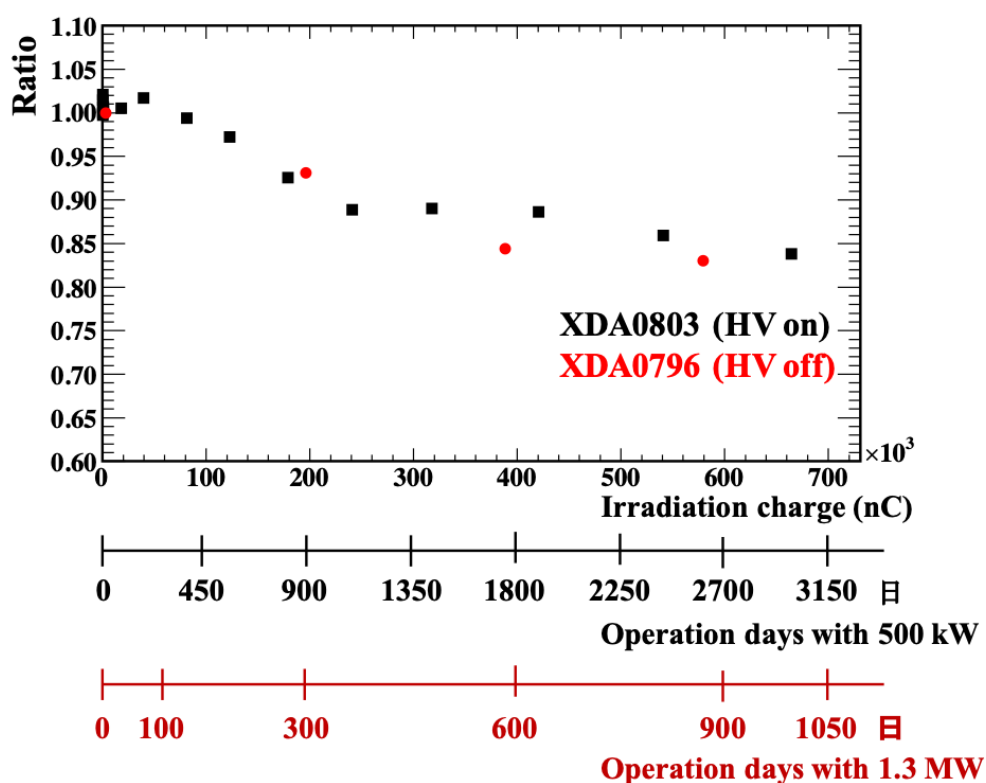


Fig.4. The irradiation charge dependence of the signal yield of the EMT. The horizontal axis is same to the Figure 3. The vertical axis is normalized so that the initial signal yield is 1. Black and red indicate the HV applying condition, corresponding to HV on and HV off, respectively.

§4. Summary

The muon monitor made of Si sensors and ionization chambers has shown the excellent performance in the T2K experiment. However, it has issues of linearity and radiation tolerance for the future high-intensity beam operation. The EMT is a candidate for the muon monitor device for the high-intensity operation. The previous ELPH beam tests have shown that the linearity is sufficient and the radiation tolerance is better than that of Si. However, in the test operation at J-PARC and the ELPH beam test, the phenomenon that the signal decreased by several percent at the beginning of operation sometimes occurred.

The 3rd ELPH beam test was conducted to investigate the initial instability, the limit of radiation tolerance, and the cause of radiation deterioration. In addition, in order to measure the high-intensity beam profile, which has not been measured in the previous beam tests, an OTR monitor was introduced, and the profile measurement of the high-intensity beam was successfully performed, and the irradiation efficiency was calculated with more reliability. No initial instability was observed in the measurement results, raising the possibility of temperature dependence. It was reconfirmed that radiation resistance is sufficient. Moreover, since deterioration occurred even in HV-off, it was found that excessive electronic amplification is not the main cause of deterioration. As a result of the tests on the EMT and the bleeder circuit, the main cause of radiation deterioration was found to be at the EMT body. When only the bleeder circuit was irradiated, the signal yield increased slightly, but no abnormal values were observed in the resistance and capacitance values after irradiation, so the reason for the increased signal amount is not concluded in this beam test. In the future, it will be necessary to compare the resistance and

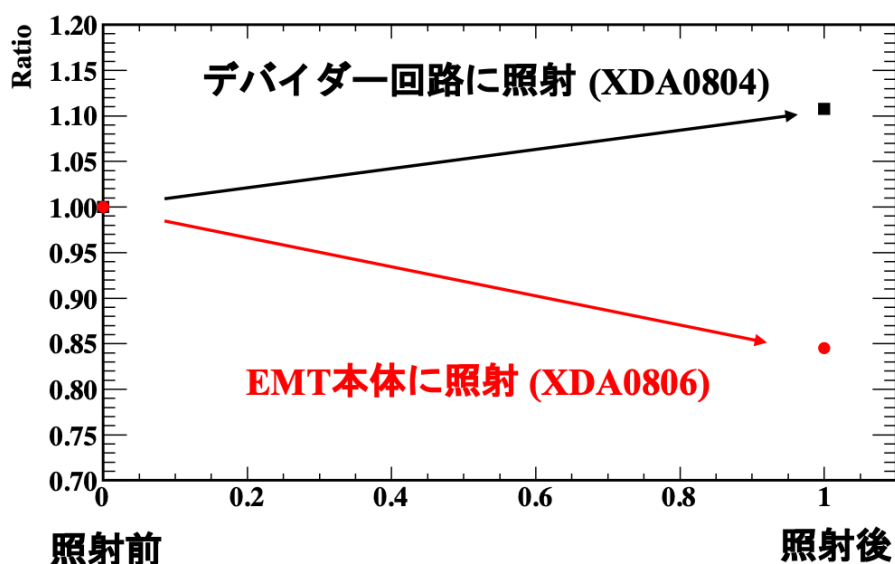


Fig.5. The irradiation charge dependence of the signal yield of the EMT. The irradiation amount is correspond to the 300 days T2K operation with 500kW beam power. The vertical axis is normalized so that the initial signal yield is 1. Red and black indicate irradiation target, which correspond to the EMT main body and the bleeder circuit, respectively.

capacitance values before and after irradiation.

As a result of the measurement, we conclude that EMT has sufficient performance as a sensor for the next muon monitor in T2K experiment, and we were able to clarify the points that should be understood in order to use EMT stably for a long time.

Acknowledgment

The authors are grateful to the ELPH accelerator staffs for supplying a superb beam, especially to Shigeru Kashiwagi and Atsushi Tokiyasu for their great support and coordination. This work was supported by MEXT KAKENHI Grant Numbers 25105002, 16H06288, 15J01714, and 17J06141, and the U.S.-Japan Cooperation Program in High Energy Physics.

References

- [1] K. Abe *et al.*, Nucl. Instr. Meth. A **659** 106-135 (2011)
- [2] K. Matsuoka *et al.*, Nucl. Instr. Meth. A **624** 591-600 (2010)
- [3] K. Suzuki *et al.*, Prog. Theor. Exp. Phys. **2015** 5, 053C01 (2015)
- [4] K. Abe *et al.*, arXiv:1609.04111 (2016)
- [5] K. Abe *et al.*, arXiv:1908.05141 (2019)
- [6] Y. Ashida *et al.*, Prog. Theor. Exp. Phys. **2018** 10, 103H01 (2018)
- [7] T. Honjo, master thesis in Osaka City University (2021)
- [8] N. Izumi, master thesis in Tokyo University of Science (2021)
- [9] K. Takifuji, master thesis in Tohoku University (2022)
- [10] H. Nakamura, master thesis in Tokyo University of Science (2022)

(ELPH Experiment : #3016)

Production of Carrier Free Lu-177 by Photonuclear Reaction

K. Akiyama¹, A. Tamura¹, H. Kikunaga², and S. Kubuki¹¹*Department of Chemistry, Tokyo Metropolitan University, Hachioji, 192-0397*²*Research Center for Electron Photon Science, Tohoku University, Sendai, 982-0826*

The production of ¹⁷⁷Lu by the irradiation of HfO₂ as a target material with bremsstrahlung with a maximum energy of 30 to 60 MeV is reported. ¹⁷³Hf, ¹⁷⁵Hf, ¹⁸¹Hf, ¹⁷⁷Lu, and ⁸⁹Zr were observed in the irradiated HfO₂ from γ -ray measurement and the production yield of ¹⁷⁷Lu at 30, 40, 50, 55, 60 MeV is found to be $(4.3\pm 0.6)\times 10^2$, $(5.7\pm 0.5)\times 10^3$, $(1.32\pm 0.03)\times 10^4$, $(1.04\pm 0.03)\times 10^4$, and $(1.60\pm 0.04)\times 10^4$, respectively. Estimated relative radioactivity of (^{177m}Lu/¹⁷⁷Lu) was found to be less than 0.321%.

§1. Introduction

Lu-177 whose half-life is about 7 day is a kind of the radioisotopes of Lu belonging to lanthanide elements is one of the promising radionuclides applied for radiopharmaceuticals [1], and is possible to apply for both diagnosis and treatments in terms of emitting both β particles and γ ray. There are two main pathways to produce ¹⁷⁷Lu using reactor neutrons. One is called “Direct method” by ¹⁷⁶Lu (n, γ) ¹⁷⁷Lu reaction and another is “Indirect method” to produce ¹⁷⁷Lu as a daughter nuclide by β decay of ¹⁷⁷Yb obtained from ¹⁷⁶Yb (n, γ) ¹⁷⁷Yb reaction. In the direct method, the specific radioactivity of ¹⁷⁷Lu is low due to the presence of a large amount of stable isotope of Lu used as a target, and in the indirect method, the isolation of Lu from Yb is difficult because of the difficulties in the mutual separation of each lanthanide. Recently, it is suggested to produce ¹⁷⁷Lu from ¹⁷⁸Hf by the photonuclear reaction using an electron linear accelerator because of the simple chemical separation of Hf and Lu in addition to the possibility of the suppression of the nuclear isomer of ^{177m}Lu which has about 160 days half-life [2]. In this study, we try to produce ¹⁷⁷Lu from natural HfO₂ by the photonuclear reaction which has been demonstrated in a small number of reports and with the higher energy range of irradiation already reported together with the quantification of the radioactivity of the by-product of ^{177m}Lu. In addition, we try to develop the separation method of Lu from Hf without hydrofluoric acid (HF) which is toxic to the human body.

§2. Experimental

About 0.1 g of HfO₂ targets were formed into 9 faimm pellets and wrapped in high-purity Al foil. These samples were sealed in a quartz tube under reduced pressure and then were irradiated with bremsstrahlung with a maximum energy of 30 to 60 MeV for 10 minutes using an electron linear accelerator at the Research Center for Electron Photon Science (ELPH) in Tohoku University. After the

irradiation, the γ rays emitted from the samples were measured by a **Ge** semiconductor detector, and the radioactivity of each nuclide was estimated. Concentrated nitric acid was added to irradiated **HfO₂** and stirred. These samples were centrifuged for the separation of ^{177}Lu , and the supernatant was filtered by membrane filters and then measured by **Ge** detector.

§3. Results and Discussion

As the results of γ -ray measurement, the production of ^{173}Hf , ^{175}Hf , ^{181}Hf , ^{177}Lu , and ^{89}Zr were confirmed. Figure 1 shows the production yield of each nuclide produced in the photonuclear reaction as a function of the maximum energy of bremsstrahlung. It is found that the production yield of all these nuclides were basically increased with increase of the maximum energy except for the ^{181}Hf .

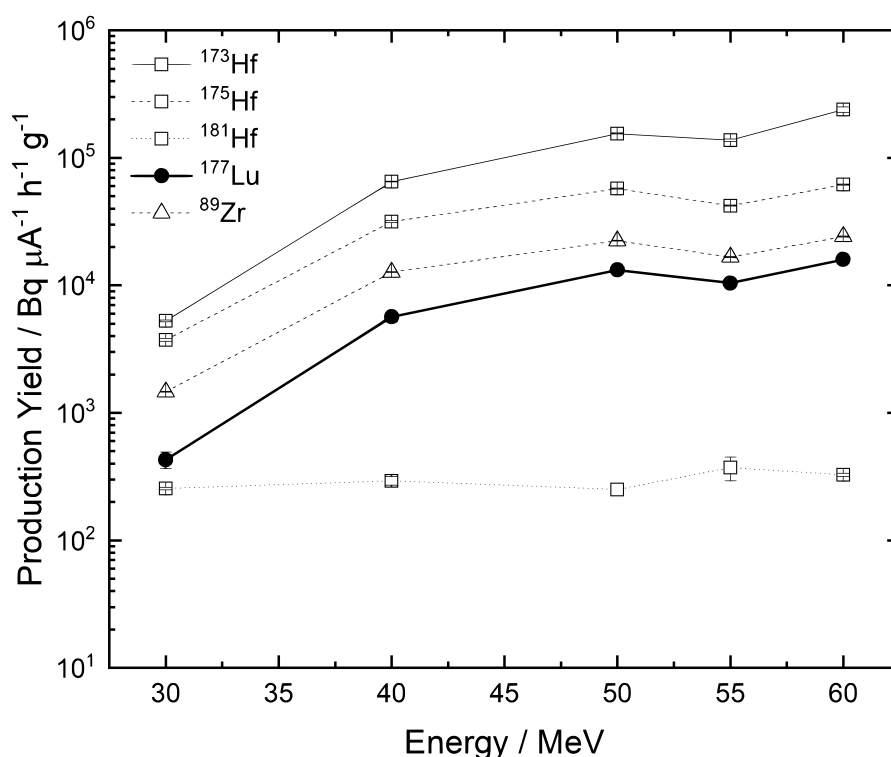


Fig.1. Production yield of nuclides observed in this study

Inagaki *et al.*, reported the production of ^{177}Lu by bremsstrahlung with a maximum energy from 20 to 40 **MeV** [3]. The evaluated production yield at 40 **MeV** from their reported data is about $4.25 \pm 0.07 \times 10^3$ **Bq $\mu\text{A}^{-1} \text{h}^{-1} \text{g}^{-1}$** and is found to be almost consistent with our observed production yield. Figure 2 shows the decay curve of the 208 **keV** γ -ray emitted from ^{177}Lu and ^{177m}Lu with 50 **MeV** irradiation. It is required that the production of ^{177m}Lu should be suppressed because of their long half-life. In this time, we could not observe the contribution of ^{177m}Lu to this decay curve. The relative radioactivity of ^{177m}Lu to ^{177}Lu ($^{177m}\text{Lu}/^{177}\text{Lu}$) was found to be less than 0.321%. In the extraction of **Lu** from **HfO₂** target irradiated at 50 **MeV** bremsstrahlung in concentrated nitric acid solution, only about 1% of the ^{177}Lu found in the irradiated sample could be recovered in the filtered supernatant. This result indicates

that the rate of releasable ^{177}Lu produced by photon irradiation from strong bonding HfO_2 is estimated to be about 1%. In near future, we plan to develop a method of dissolving HfO_2 without using toxic HF .

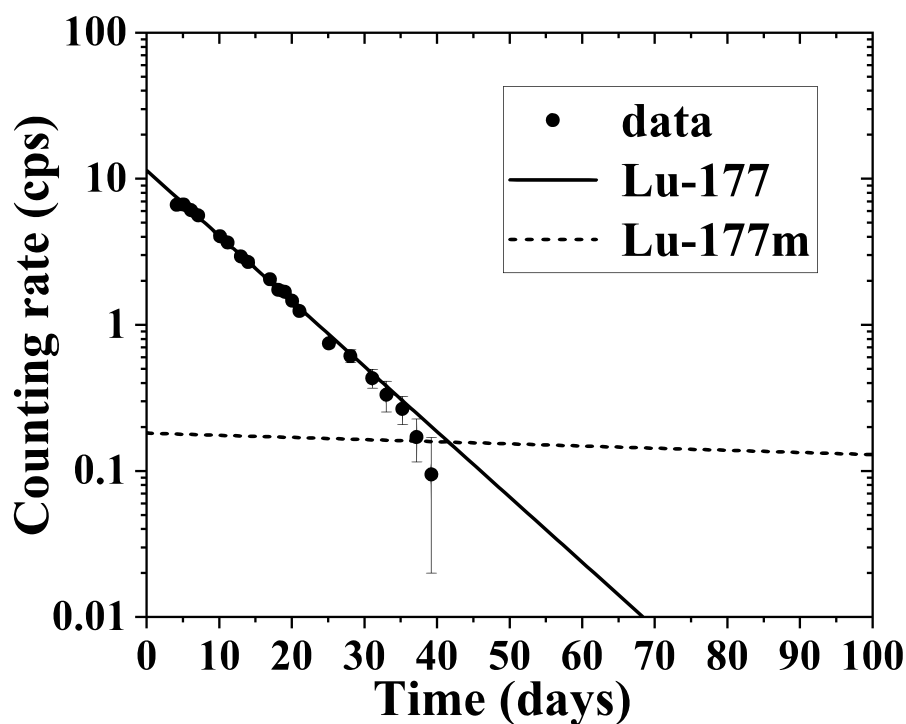


Fig.2. Decay Curve of 208 keV γ -ray

Acknowledgment

We deeply thank to the facility staffs of research center for electron photon science at Tohoku University for supplying the high-quality electron beam. And also we thank to Doctor Y. Honda for helping us in the sample irradiation.

References

- [1] S. Watanabe *et al.*: J. Radioanal. Nucl. Chem. **303** (2015) 935.
- [2] A. G. Kazakov *et al.*: Molecules **27** (2022) 3179.
- [3] M. Inagaki *et al.*: J. Radioanal. Nucl. Chem. **322** (2019) 1703.

(ELPH Experiment : #2980)

Radiation tolerance tests with electron beam for Belle II silicon strip vertex detector

Y. Sato¹, F. Otani², K. Hara¹, T. Higuchi³, A. Ishikawa¹, K. Nakamura¹,
Y. Onuki², T. Shimasaki², H. Sudo², H. Tanigawa¹, T. Tsuboyama¹,
Y. Uematsu², and Z. Wang²

¹*High Energy Accelerator Research Organization (KEK), Tsukuba 305-0801, Japan*

²*Department of Physics, University of Tokyo, Tokyo 113-0033, Japan*

³*Kavli Institute for the Physics and Mathematics of the Universe (WPI), University of Tokyo,
Kashiwa 277-8583, Japan*

The Belle II experiment [1] is located at SuperKEKB at KEK, Tsukuba, Japan, a B meson factory facility taking data at the $\Upsilon(4S)$ resonance with the electron-positron collision. The vertex detector (VXD) is the innermost tracking device of the Belle II detector and consists of two layers of the pixel detector and four layers of the silicon strip detector (SVD) [3].

The main source of background in the SVD comes from the electromagnetic showers produced by the beam particles hitting the wall of the beam pipe. A dominant fraction of the background is electron and positron with energies of the order of 10 to 100 MeV. They cause displacement of the silicon lattice atoms, which changes the electrical properties of the sensor.

The expected radiation dose on the innermost SVD layer for 10 years of the Belle II operation with the designed luminosity is 20 kGy. We investigate the radiation tolerance of the SVD sensor by irradiating the 90 MeV electron up to 200 kGy of the radiation dose.

In order to evaluate the radiation tolerance of the SVD sensor, we measure the leakage current, bulk capacitance, and inter-strip capacitance. The measurement results are being analyzed.

Acknowledgment

We greatly appreciate the staff of ELPH for their extensive support and stable beam operation. This work was supported by JSPS KAKENHI Grant Numbers JP19H01912, JP19H00692.

References

- [1] T. Abe *et al.* [Belle-II], [arXiv:1011.0352 [physics.ins-det]].
- [2] K. Akai *et al.* [SuperKEKB], Nucl. Instrum. Meth. A **907** (2018), 188-199 doi:10.1016/j.nima.2018.08.017 [arXiv:1809.01958 [physics.acc-ph]].
- [3] K. Adamczyk *et al.* [Belle-II SVD], JINST **17** (2022) no.11, P11042 doi:10.1088/1748-0221/17/11/P11042 [arXiv:2201.09824 [physics.ins-det]].

(ELPH Experiment : #2500, #2501)

The status report of LEPS2-solenoid experiment in 2021

Atsushi Tokiyasu¹ and LEPS2 collaboration

¹Research Center for Electron Photon Science, Tohoku University, Sendai, 982-0826

At SPring-8, the LEPS2 solenoid experiment is studying hadron photoproduction using intense photon beam with the energy ranging from 1.3 to 2.9 GeV and a large solid angle solenoid spectrometer. In FY2021, as in FY2020, the performance of the detectors using liquid hydrogen and liquid deuterium was evaluated and physics data were obtained. Data collection is progressing well and we expect to report physical results soon.

§1. Introduction

At the LEPS2 experimental facility at SPring-8, hadron photoproduction experiments are being performed using intense photon beams of 10^6 to 10^7 cps produced by backward Compton scattering. The energy of the photon beam is ranging from 1.3 to 2.9 GeV, which is especially suitable for the production of hadrons containing strange quarks. High-momentum particles from hadron-producing reactions are detected by the LEPS2 solenoid spectrometer placed surrounding the physics target.

Shown in the Figure 1, the LEPS2 solenoid spectrometer consists of a solenoidal electromagnet with a strength of 1 Tesla, a Start Counter for data acquisition, a Time Projection Chamber for track measurements, a Resitive Plate Chamber for time-of-flight measurements, a Sampling Calorimeter for neutral particle detection, and an Aerogel Cherenkov Counter for particle identification. In addition, a Resitive Plate Chamber for Time-Of-Flight measurements and the Neutron Counter for neutron measurements are located in downstream of the detector.

The first physics goal of the LEPS2 solenoid experiment is to search for the K^-pp bound states using photo-induced reactions. K^-pp bound states are a new type of nuclei consisting of an \bar{K} meson and two protons. To obtain further information on the internal structure of the K^-pp bound states, it is essential to conduct search experiments using complementary probes, i.e., photon beams. We plan to identify the $\gamma + d \rightarrow K^0 + \Lambda + p$ reaction and to search for the peak structure associated with K^-pp bound state production from the invariant mass distribution of Λ and proton.

§2. Update from the previous FY

In 2021, a neutron counter wall (NC) with the size of 3800 (hori) \times 1820 (vert) \times 152 mm was newly installed (Fig. 2-(a)). The neutron counter wall consists of two layers of 24 plastic scintillators with four photomultitubes attached to each side.

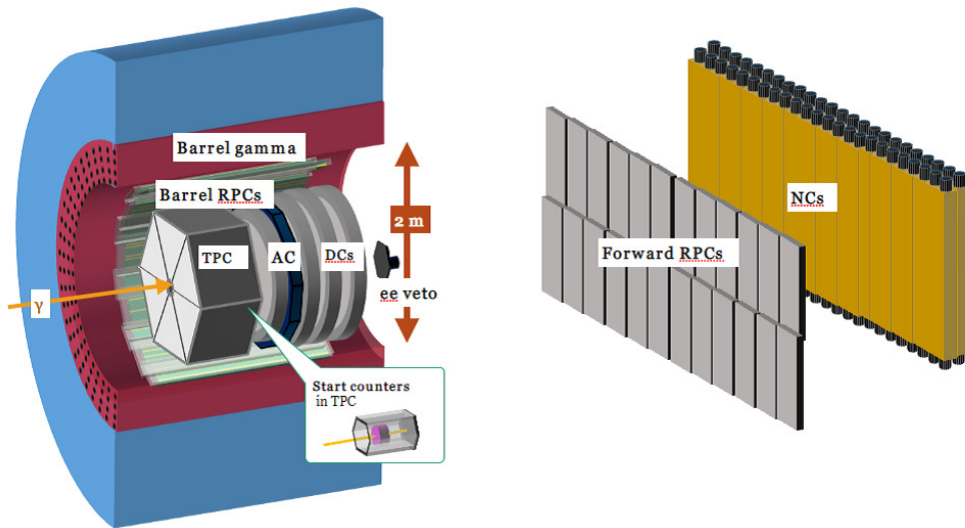


Fig.1. The LEPS2 solenoid spectrometer

The performances of NC were evaluated with photon beam injected on the liquid hydrogen and liquid deuterium target [1]. Figure 2-(b) shows the time distribution of NC. Time resolution of approximately 150 ps and position resolution of approximately 30 mm are achieved.

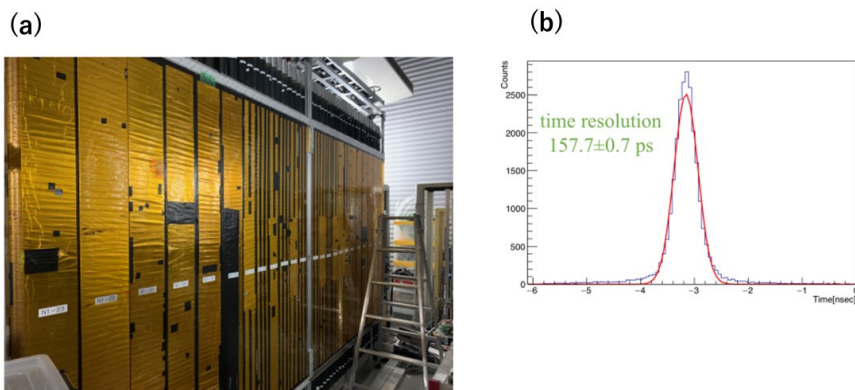


Fig.2. (a) A picture of the neutron counter wall. (b) Time distribution of neutron counter obtained with beam data.

In addition to that, beam profile monitor was installed in the upstream of the beam dump [2]. Beam profile monitor (BPM) was composed of a scintillator plate and a 64ch(8×8) MPPC array. Upstream of BPM, copper plate was installed as e^+e^- converter. In addition, a thin scintillator plate was installed to reject the detection of the charged particles.

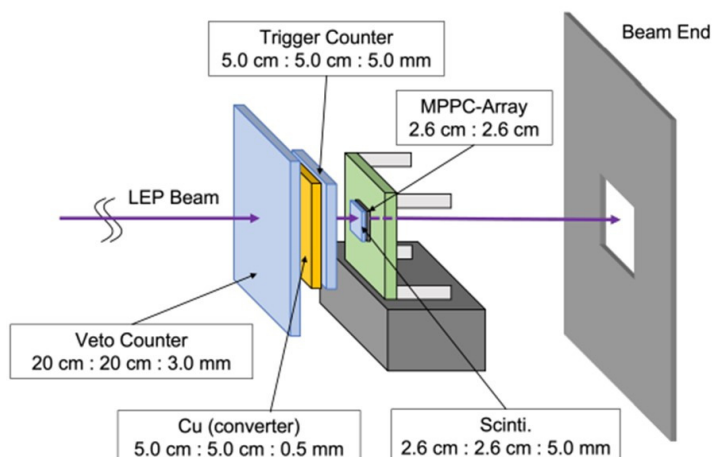


Fig.3. Over view of the beam profile monitor.

Figure 4 show the beam profile obtained with BPM. The obtained beam size was found to be almost consistent with the calculated value. BPM enables us to monitor the beam position and size during collecting the data.

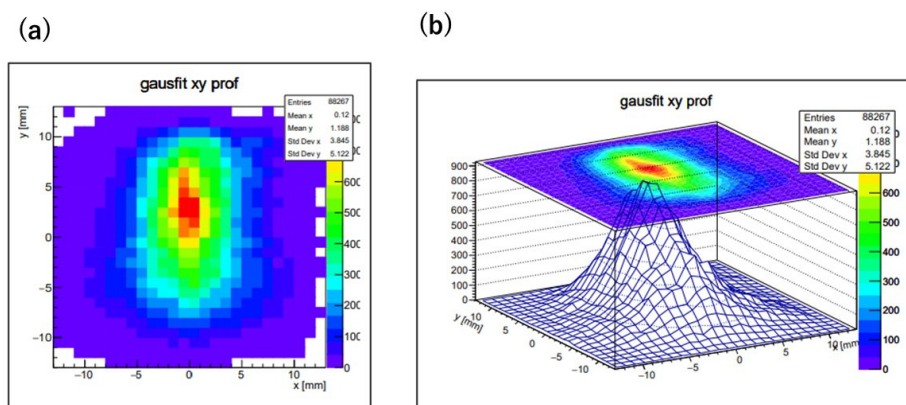


Fig.4. The beam profile with BPM. (a) 2-dimensional scatter plot. (b) 3-dimensional scatter plot.

§3. Collected data

In the LEP2 solenoid experiment, physics data acquisition using liquid hydrogen and liquid deuterium targets is being continued from the previous fiscal year. Due to the rising price of electricity, the current of the solenoid electromagnets was reduced from 4000A to 3600A. We have confirmed that this

change will not have a significant impact on the physical results we seek. We evaluated the performance of detectors by using this data set. It was confirmed that almost all detectors were operating as expected.

§4. Result

The masses of charged particles were reconstructed from momentum from the tracking with TPC and velocities from the Time-Of-Flight measured with RPC. We successfully observed a clear locus of protons and pions in the scatter plot of momentum and calculated mass (Fig.5).

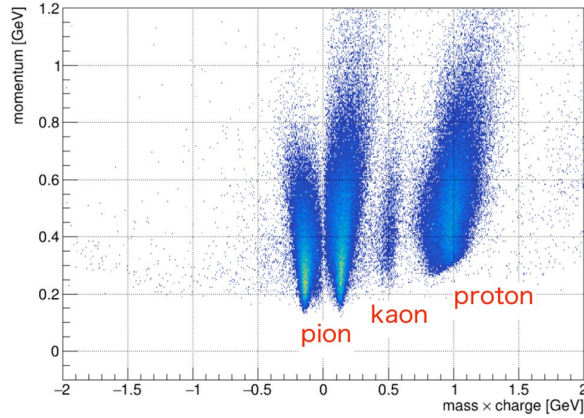


Fig.5. 2-dimensional scatter plot of momentum vs mass times charge.

We selected pairs of proton and π^- , and obtained their invariant mass spectrum and observed the peak of the lambda hyperon (Fig.6-(a)). We also identified a proton, and the missing mass was calculated assuming that the target proton was stationary. As a result, we succeeded in observing the π^- , η , and ω meson peaks (Fig.6-(b)). These results show that the performance of the detectors are consistent with the expected value of the simulation.

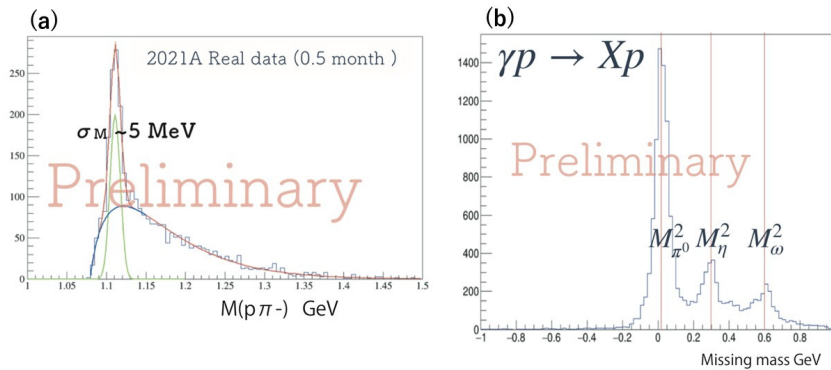


Fig.6. (a) Invariant mass spectrum of proton and π^- (b) Missing mass spectrum of γ and proton.

§5. Summary

At SPring-8, we are conducting the LEPS2 solenoid experiment. We started to take data of physics with a liquid hydrogen and a liquid deuterium target. We measured the momenta and identified the particles by the detectors installed inside the solenoid magnet. We continued the evaluation of performance of the detectors by using the physics reaction like Λ production or meson production. The first goal of the LEPS2-solenoid experiment is a search for the K^-pp bound state. We are analyzing the collected data, and physics results will be reported near future.

Collaboration

The LEPS2-Solenoid experiment is being conducted in cooperation with the following institutions: Tohoku University, Osaka University, Kyoto Sangyo university, Gifu University, Chiba University, Korea University, RIKEN, University of Saskatchewan and JINR.

References

- [1] T. Nobata : Master thesis in Tohoku University (2021)
- [2] Y. Shibata : Master thesis in Gifu University (2021)

Improvement of a Mo/Si multi-layer mirror for the high-energy γ beam production by X -ray Compton scattering

Norihito Muramatsu¹, Schin Daté^{2,3}, Tetsuo Harada⁴, Kazuhiro Kanda⁴,
Manabu Miyabe¹, Shuji Miyamoto^{5,4}, Haruo Ohkuma^{2,6}, Masahiro Okabe¹,
Hajime Shimizu¹, Shinsuke Suzuki^{3,2}, Atsushi Tokiyasu¹,
and Takeo Watanabe⁴

¹Research Center for Electron Photon Science, Tohoku University, Sendai, Miyagi 982-0826, Japan

²Research Center for Nuclear Physics, Osaka University, Ibaraki, Osaka 567-0047, Japan

³Japan Synchrotron Radiation Research Institute (SPring-8), Sayo, Hyogo 679-5198, Japan

⁴Laboratory of Advanced Science and Technology for Industry, University of Hyogo, Kamigori, Hyogo 678-1205, Japan

⁵Institute of Laser Engineering, Osaka University, Suita, Osaka 565-0871, Japan

⁶Aichi Synchrotron Radiation Center, Seto, Aichi 489-0965, Japan

§1. Introduction

A high-energy γ beam is produced by Compton scattering of seed photons from an electron storage ring in the GeV energy region. A laser light is usually used as the source of seed photons, but we are developing a new method to inject X -rays into the storage ring for the purpose to increase the γ beam energy significantly. In our method, X -rays are obtained from an undulator placed at a storage ring and reflected backwardly into the original ring [1]. The 180° reflection of X -rays can be done by using a multi-layer mirror. At the moment, a Mo/Si mirror is practically usable with high reflectance for the energies around 92 eV.

Development of necessary techniques and demonstration of X -ray Compton scattering are now conducted at BL07A [2] of NewSUBARU. In this beamline, a short undulator (total length: 2.28 m, period length: 7.6 cm) is installed in the straight section. The maximum energy of a γ beam produced by the Compton scattering of 92 eV X -rays reaches 0.58 and 1.02 GeV depending on the electron energy setting at 1 and 1.5 GeV, respectively. We have set up a large mirror chamber at BL07A to place the Mo/Si multi-layer mirror with automatic stepping-motor stages in a vacuum of 10^{-6} Pa [3]. For measuring profiles and intensities of both radiated and reflected X -rays, a wire scanner has been prepared about 3 m upstream of the mirror chamber. Now we are developing the Mo/Si multi-layer mirror to achieve a good focus at the Compton scattering point with high reflectance. This report describes the status of this development.

§2. Development of an improved mirror

A prototype of the multi-layer mirror was made by using a substrate of a low thermal expansion glass ceramic (Zerodur) with 50 periodic layer coating of Mo and Si. Its reflective surface was cylindrically polished to make a focus on the electron beam 16.7 m upstream. This cylindrical surface was made by bending the substrate with application of stress at two edges, then polishing a surface flatly, and finally releasing the stress [4]. However, the obtained curvature radius was 14.4 m in the measurement by an ultrahigh accurate 3D profilometer [5]. In addition, the RMS value of surface roughness was measured to be 0.99 nm in $2 \times 2 \mu\text{m}^2$ by using an atomic force microscope (AFM). It was not very good compared with the reflecting wavelength of 13.5 nm. We also tested a temperature rise of the multi-layer mirror by irradiating undulator X -rays at BL07A. The maximum temperature reached 190°C. It turned out that heat conductance from the mirror to the water-cooled holder was bad in a vacuum. This may possibly cause a distortion of the mirror surface, lowering the ability of reflected X -ray focusing.

Thus, we have produced a new mirror with a Silicon substrate, which has an area of $50 \times 50 \text{ mm}^2$ and a thickness of 16 mm. This substrate was chosen for better heat conductance and hardness against surface distortion. The reflective surface was polished in the cylindrical shape with an ideal curvature radius of 16.7 m by applying magneto-rheological finishing. Removal of heat was further improved by putting a thin Indium sheet to the gap between the mirror substrate and the mirror holder. The surface condition of this new mirror was examined in a way similar to the old mirror tests. The RMS value of surface roughness was improved to 0.2 nm in an area of $80 \mu\text{m}^2$. The surface accuracy was also excellent, showing that the deviation from the designed cylindrical shape was within 134 nm in an effective area of $45 \times 45 \text{ mm}^2$. Fifty periodic layers of Mo and Si were finally made on the reflective surface.

The performance of the produced mirror was tested at BL10 of NewSUBARU. Figure 1 shows the reflectance of X -rays around the energy of 92 eV. Different colored lines indicate the reflectance values at seven incident points on the mirror. The maximum reflectance was 65.8% in the case of injection at the mirror center. This value was close to the design, and higher than the reflectance of the old mirror (54.2%). A diffusion component of the reflected X -rays was also confirmed to be small enough in the case of the new mirror.

§3. Beamline test of the developed mirror

The new multi-layer mirror was installed inside the mirror chamber at BL07A of NewSUBARU and tested by an X -ray beam from the short undulator. The undulator gap was adjusted to emit 92 eV X -rays as the first harmonic radiation. The X -ray intensity reaches 1.5×10^{16} photons/sec/mm²/mrad²/0.1%bw at the electron beam energy and current of 1 GeV and 300 mA, respectively. This X -ray beam was backwardly reflected at the Mo/Si mirror to check its performance. Both the profiles of radiated and reflected X -ray beams were measured at the wire scanner, where a W wire of 0.2 mm diameter was slowly moved by an air cylinder. When X -rays hit the wire, a micro current arises by photoelectric effect. We measured the wire position and the micro current simultaneously by using a potentiometer and a picoammeter for obtaining the profile.

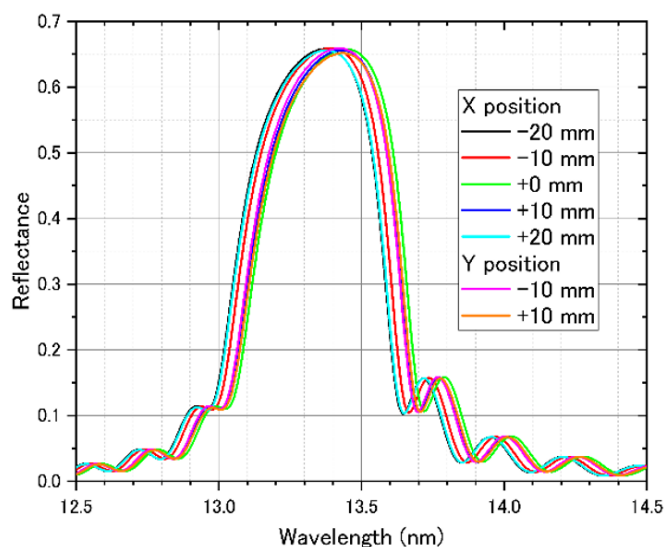


Fig.1. Reflectance of a developed Mo/Si multi-layer mirror with a Silicon substrate.

Figure 2 shows the measured profiles that include both radiated and reflected X -rays. Besides the radiated X -ray peak, a reflected component clearly appeared with a small shift due to the mirror angle setting. The peak height ratio of reflected to radiated components was about 20%, which was significantly improved from the old mirror case. This behavior can be explained by taking into account the fraction of the first to higher harmonic radiation at the undulator, the ratio of X -ray band widths of the mirror reflection to the undulator radiation, and the reflectance of the Mo/Si multi-layer mirror. The observed ratio of 20% was unchanged even after the X -ray irradiation of a few days, indicating no damage by temperature rise and radiation. The focussing status of the reflected X -ray beam can be recognized by comparing the width of the reflected beam profile with that of the incident beam from the undulator. If the two widths are the same as each other, the reflected beam is being focused at the Compton scattering point. Now we are precisely inspecting the profile data, but no big change of the width has been observed in Fig. 2, which shows the vertical profile. During the performance test of the new multi-layer mirror, it was also observed that the peak position of the reflected component moved in proportion to the amount of mirror angle change. Therefore, it turned out that the multi-layer mirror angles or the direction of reflected X -ray beam was easily adjustable by operating the stepping motor stages which the water-cooled mirror holder was mounted on.

§4. Summary

We have developed a Mo/Si multi-layer mirror to reflect X -rays backwardly for Compton scattering at the electron storage ring. The maximum reflectance reaches 65.8% for the X -rays of 92 eV, showing excellent surface roughness and cylindrical curvature precision. We clearly observed an expected amount of reflected X -rays in a test of the new mirror with a beam from the undulator at BL07A of NewSUBARU. We plan to demonstrate the production of X -ray Compton scattering at this beamline.

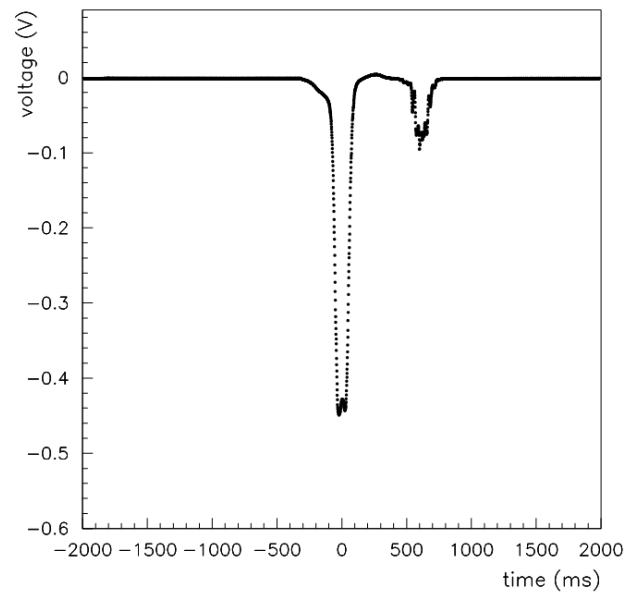


Fig.2. Vertical profiles of X-ray beams which was radiated from the undulator (left peak) and reflected by the multi-layer mirror (right peak).

Acknowledgment

This research is supported in part by Grant-in-Aid for Challenging Research (Pioneering) No. 18H05325 / 20K20344, Scientific Research (B) No. 22H01225, and Challenging Research (Exploratory) No. 22K18707.

References

- [1] <http://www.rcnp.osaka-u.ac.jp/mura/kaitaku/>
- [2] S. Tanaka, S. Suzuki, T. Mishima and K. Kanda, *J. Synchrotron Rad.* **28** (2021) 618.
- [3] N. Muramatsu, *et al.*, *J. Particle Accelerator Society of Japan* Vol.**16** No.3 (2019) 154.
- [4] M. Okabe, Master thesis (Tohoku University, 2020).
- [5] N. Muramatsu, *et al.*, *ELPH Annual Report 2020* (Tohoku University, 2022) 49.

(ELPH Experiment : #2984)

Performance evaluation of the Intermediate Tracker for sPHENIX

G. Nukazuka¹, C.W. Shih², Y. Sugiyama³, Y. Akiba¹, H. En'yo^{1,4}, T. Hachiya³,
S. Hasegawa⁵, M. Hata³, H. Imai^{4,6}, M. Morita³, I. Nakagawa^{1,4},
Y. Nakamura⁶, G. Nakano⁶, Y. Namimoto³, R. Nouicer⁷, M. Shibata³,
M. Shimomura³, R. Takahama³, K. Toho⁸, M. Tsuruta⁸, and M. Watanabe³

¹*RIKEN BNL Research Center, Brookhaven National Laboratory, Upton, New York 11973-5000, USA*

²*Department of Physics, and Center of High-energy and High-field Physics, National Central University, Chungli, Taiwan*

³*Nara Women's University, Kita-uoya Nishi-machi Nara 630-8506, Japan*

⁴*RIKEN Nishina Center for Accelerator-Based Science, Wako, Saitama 351-0198, Japan*

⁵*Advanced Science Research Center, Japan Atomic Energy Agency, 2-4 Shirakata Shirane, Tokai-mura, Naka-gun, Ibaraki-ken 319-1195, Japan*

⁶*Physics Department, Rikkyo University, 3-34-1 Nishi-Ikebukuro, Toshima, Tokyo 171-8501, Japan*

⁷*Brookhaven National Laboratory, Upton, New York 11973*

⁸*Research Center for Electron Photon Science, Tohoku University, Sendai, 982-0826*

The silicon strip barrel detector, namely the intermediate tracker (INTT), is one of the tracking detectors in the sPHENIX detector complex at the Relativistic Heavy Ion Collider in Brookhaven National Laboratory. Using the positron beam with a momentum of 1 GeV at the ELPH gamma-ray irradiation room, we evaluated the performance of the mass production INTT ladders. The energy deposit curve showed that noise contamination to the minimum ionization particle's peak is about 0.3%. This feature enables us to operate the detector with a low threshold, leading to high detection efficiency. The detection efficiency of one of the ladders was found to be $99.33 \pm 0.04(\text{stat}) \pm 0.06(\text{sys})\%$, and it was uniform over the silicon cells.

§1. Introduction

sPHENIX collaboration will be launched in 2023 at the Relativistic Heavy Ion Collider in Brookhaven National Laboratory for the investigation of Quark-Gluon Plasma and cold-QCD. The sPHENIX detector consists of the micro-vertex detector (MVTX), the intermediate tracker (INTT), the time projection chamber (TPC), the electromagnetic calorimeter, the superconducting magnet, and the hadron calorimeter.

§2. INTT

INTT is a silicon strip barrel detector consisting of two layers of silicon strip sensors surrounding the collision point seven to ten centimeters away (Figure 1). Hits detected by this detector are used not only for interpolation of tracking between MVTX and TPC but also bunch-crossing identification to suppress event-pileup background thanks to the best timing resolution of all tracking detectors in sPHENIX. 24 or 32 INTT ladders form the inner and outer layers. The INTT ladder (Figure 2) consists

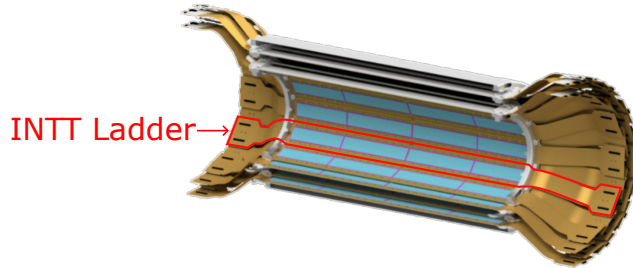


Fig.1. A half part of the INTT barrel. The inner and the outer barrels consist of 24 and 32 INTT ladders, respectively. The red box indicates an INTT ladder.

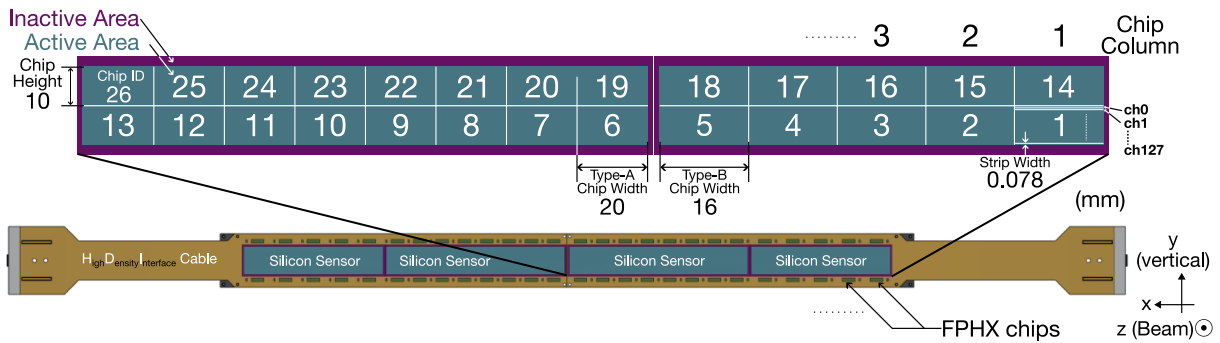


Fig.2. The INTT ladder consists of two types of silicon sensors, FPHX chips, High-Density Interconnect cable, and CFC stave. The sensors are divided into 10 or 16 cells. The silicon cells have 128 strips with 78 μm width and 320 μm thickness. The x-, y-, and z-axes in the test beam experiment are also shown.

of two types of silicon sensors, FPHX read-out chips [1], High-Density Interface (HDI) cable, and Carbon Fiber Composite (CFC) stave. Silicon sensor type-A and type-B are divided into sixteen or ten cells, respectively, and each cell has 128 silicon strips with a width of 78 μm and a thickness of 320 μm . An FPHX chip reads signals from strips in a cell, converts the signal voltage to digital information with 3-bit ADC, and sends it to the read-out card (ROC) through the HDI cable and the newly developed extension cable [2]. In the data analysis discussed in section 4.2, pairs of the silicon cells in the same column, for example, chip one and fourteen, were treated as single silicon chip columns. The left and right halves of the INTT ladder are the same structure but operated independently.

We evaluated the performance of the INTT silicon sensor from radiation measurements at the test benches and two test beam experiments and obtained some significant results: sensitivity to the beam position, the peak produced by minimum ionization particles (MIPs), signal-to-noise (S/N) ratio, and so on. Thanks to the excellent S/N ratio, the sensor is expected to show almost 100 % detection efficiency

for MIPs. However, $96.0 \pm 0.5\%$ was the best performance with prototype half ladders in the second test beam experiment performed in 2019 [3]. Therefore, before launching sPHENIX, performance evaluation and more investigations on the detection efficiency must be done to understand the detector better. The experiment described in the following section tested the mass-production ladders.

§3. The experiment

We installed the whole setup (Figure 3) on the 23° beamline in the ELPH gamma-ray irradiation room and irradiated the setup with a positron beam with a momentum of about 1 GeV. The primary gamma-ray beam and tungsten production target of $200\ \mu\text{m}$ thickness produced electron-positron pairs, and positrons were led to our beamline. Then right half of the INTT ladders in the dark box were operated and detected hits made by the beam. As trigger detectors, two plastic scintillators with the same

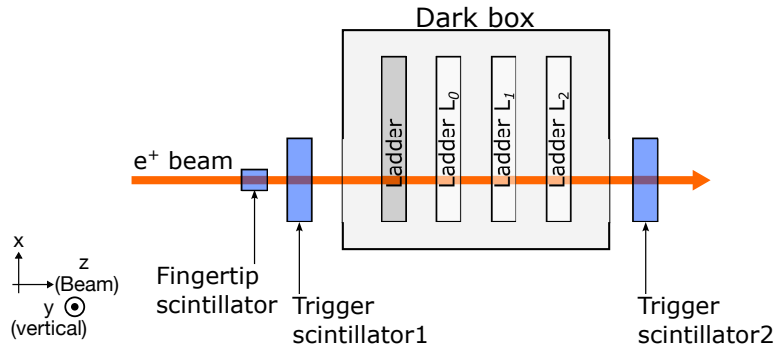


Fig.3. The setup for the test beam experiment at ELPH. The dark box, which contained the INTT ladders inside, was installed on the positron beam line. Two trigger scintillators and a fingertip scintillator were set upstream and downstream of the dark box. The x-, y-, and z-axes are also shown.

cross-sectional area as the silicon sensors of the half-ladder were installed just upstream or downstream of the dark box. We additionally installed a fingertip scintillator at the most-upstream position of the setup for additional data selections in the analysis but not as the trigger. Three INTT ladders, namely L0, L1, and L2 from the upstream, that showed good performance were connected to the ROC, and the ROC was connected to slow control and read-out electronics for operation. Nuclear Instruments Modules did some processes for signals from the scintillators, for example, digitization, generation of trigger signals, and trigger input to the INTT Front-End Module (FEM). The FEM module processed INTT data only when having trigger signals.

§4. Results

As a typical silicon detector, the INTT is required to demonstrate high detection efficiency, which can be achieved by good S/N ratio. As shown in Figures 2 and 3, the direction of the beam was set as the z-axis in the study. The y-direction points vertically from the bottom to the top, and the x-axis follows the right-handed Cartesian coordinate system.

4.1 Signal noise ratio from the energy deposit curve

Noise contamination to the MIP peak region in the energy deposit curve is one of the crucial features in performance evaluation. As already demonstrated by prototype ladders in the past experiment, tiny noise contamination is also expected for the mass production ladders under the ELPH beam test environment.

The 3-bit ADC in the FPHX chip converts the height of the signal generated in the sensor. As a preparation for the signal AD conversion process, the 8-bit DAC threshold values are preset with approximately a 4 mV step. This is called a DAC value. When the signal is processed, a corresponding DAC value is assigned and injected into a data stream as 3-bit ADC data. The ADC value is related to the energy loss of a traversing charged particle. The programmable comparator's threshold effectively allows a custom non-linear ADC.

The 3-bit ADC is designed to be handy and helps to reduce the power consumption at FPHX during the operation, while the resolution is not sufficient to observe a precise energy deposition. Thanks to the feature of the FPHX chip, ADC configuration can be changed through slow control commands. It enables us to measure the precise energy deposition, but narrow range in one shot of measurement. In order to observe a full ADC spectrum in high energy resolution, we thus performed a series of eight narrow range measurements covering slightly different DAC ranges in each measurement and scanned through the entire DAC range. Four DAC steps were assigned a single ADC value. The ADC configurations were made to have two overlapping bins between runs covering adjacent scanning ranges. The data were then combined to map out the full ADC spectrum with adequate normalization to each data in the analysis. The noise contamination below a MIP region can be estimated assuming an exponential fall function from the low ADC side.

In the data analysis, some event selections were applied, for example, the rejection of hits from the strips outside the beam spot with a too-high hit rate. Only hits on a single channel were analyzed. Hits with the highest ADC value (i.e. ADC7) were excluded from the full ADC spectrum reconstruction because the highest ADC value can be considered an overflowing value. Figure 4 shows the reconstructed full ADC distribution of chip 10 in the upstream ladder L0 obtained from eight runs. The ADC distributions were normalized by the number of entries in the two overlapping ADC bins. Then we took the mean of the overlapping bins for their entries, letting each ADC distribution of a narrow region connect smoothly with the spectrum of the adjacent region. This process was performed one by one from the smallest scan area to obtain a single energy deposit curve.

We hired a Landau-Gaussian convolution function to reproduce the MIP peak as performed elsewhere [4]. The most probable value (MPV) in the Landau component shows the typical energy deposit of MIPs. An exponential function can describe the noise contribution. The fitting result shows the experimental ADC spectrum was well reproduced by the sum of the convolution function and the exponential function, as shown in Figure 5.

Entries by MIP were dominant in the region larger than DAC 40 at the operation bias voltage of 50 V, while noise existence cannot be neglected in the lower area. The fitting result shows that MPV was

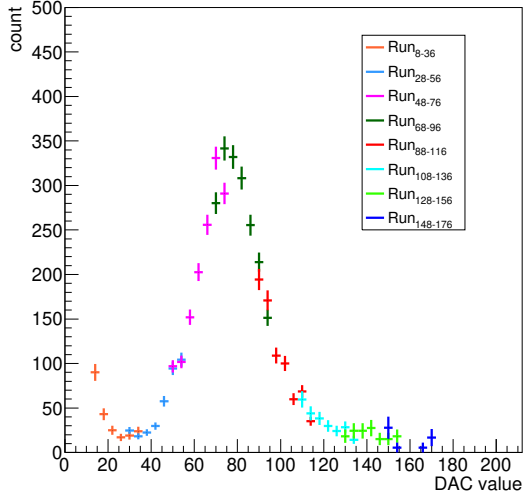


Fig.4. The ADC distribution of the eight runs after normalization. The legend indicates the scanning region of the runs.

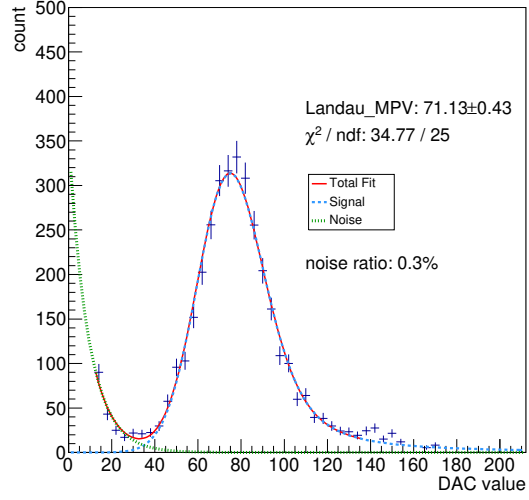


Fig.5. The energy deposit curve as a function of DAC value. Fitting to the distribution with the sum (red) of a Landau-Gaussian convolution function (dotted blue) and an exponential function (dashed green) is also shown.

71.13 ± 0.43 . The ratio of the noise component in the MIP region from DAC 40 to 136 was 0.3%, letting us conclude that the mass-production ladder was expected to be almost noiseless in the MIP region. Therefore, high detection efficiency could be expected in the MIP region.

4.2 Detection efficiency

In this study, the origin of the XY plane is defined at the central position of the sensor cells one and fourteen of the half-ladder in use. For the z-axis, the origin is given at the center of the sensor of the upstream ladder L0. Two sensor cells in the same columns are read out by individual FPHX chips and treated as a single sensor.

The adjacent fired channels in a column formed a hit cluster. The cluster position in y was determined by weighting with the ADC value of hits, as described in Equation 1:

$$\mathbf{y} = \frac{\sum_i \mathbf{E}_i \cdot \mathbf{y}_i}{\sum_i \mathbf{E}_i}, \quad (1)$$

where \mathbf{y} is the cluster position in the y-axis, i is the hit channel ID, \mathbf{E}_i and \mathbf{y}_i are the DAC value and the position of channel i in the y direction, respectively.

The upstream and downstream ladders were used for the track reconstructions, and the detection efficiency of ladder L1 was studied. In the reconstruction process, only a cluster was required on the same chip column of the two testing ladders, and no cluster in the adjacent columns of the testing ones was allowed. The tracks passing the criteria were considered as track candidates.

The residual distribution is the difference between the hit position of the tested ladder and the

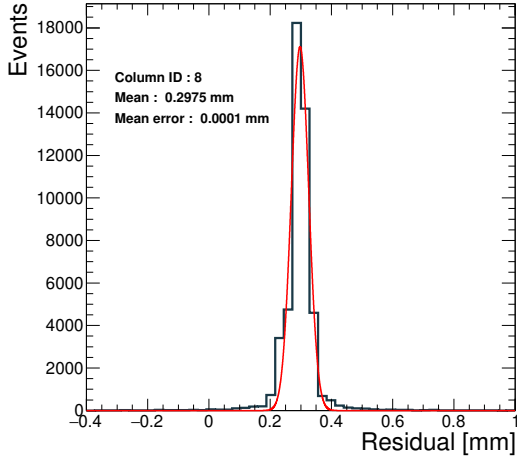


Fig.6. The residual distribution of column eight in ladder L1 before alignment correction.

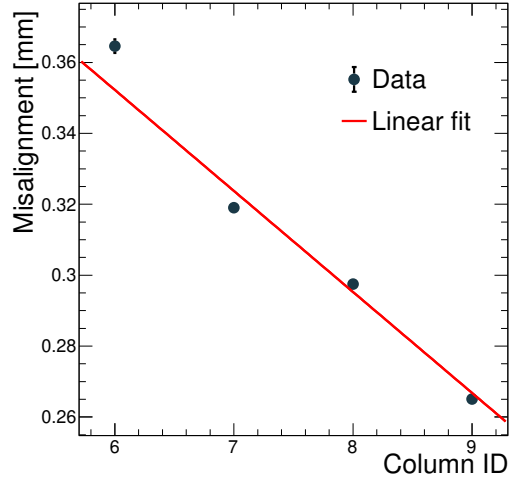


Fig.7. The amount of misalignment correction as a function of column ID. The error bars indicate the mean errors.

tracking, as defined in Equation 2

$$r \equiv (y + C_y) - y_{pred}, \quad (2)$$

where r is the residual, y_{pred} means the y position on the L1 interpolated from the tracking, y indicates the position of the cluster closest to y_{pred} , and C_y represents misalignment. Figure 6 shows the residual distribution of column eight. The non-zero value of the mean suggests the non-zero misalignment C_y . Gaussian fit to the distribution estimated the correction amount for each column, as shown in Figure 7. The dependence of the correction on the column implies that the ladders were not parallel during the experiment. The tiny none parallel components effect is ignorable as long as the track candidates are perpendicular to the ladder and traverse the same column eight throughout three ladder layers.

Some event selections were necessary to maximize the authenticity of the results. As shown in Figure 5, a tiny amount of hits with low DAC values came from noise. In the measurements, we stored hits with DAC values larger than 14. The total DAC value of clusters was required to be high enough to enhance the purity of the actual signal. We excluded the track candidates within five channels from the edges of the L1 because the misalignment might give an incorrect tracking position (**edge effect**). The limitation of the track slope within ± 0.01 was also vital to have better reliability in the analysis (Figure 8). The limitations rejected any ambiguous tracks that may not come from the beam.

The track candidates passing all the criteria mentioned above were considered good tracks. The detection efficiency of ladder L1 was then tested by checking whether a cluster was in the expected position of L1. Two cases were taken into account, ladder L1 with or without clusters. Figure 9 shows the residual distribution for the former case. The peak of the distribution was aligned to zero after the correction. The clusters within ± 0.234 mm from the interpolated point, which is the three-strip width, were considered as the hits made by the beam (residual cut). Therefore, the results can be classified into

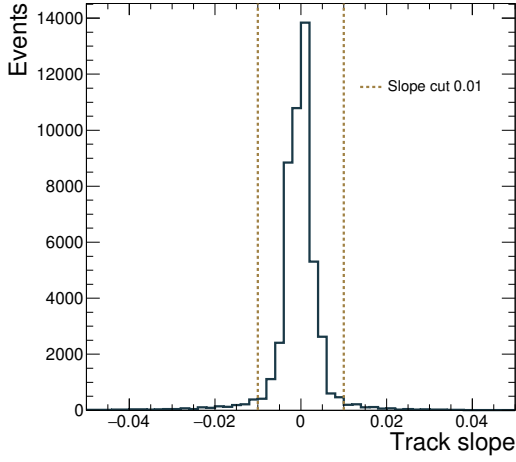


Fig.8. The slope distribution of track candidates. Tracks within slope ± 0.01 were used in the analysis.

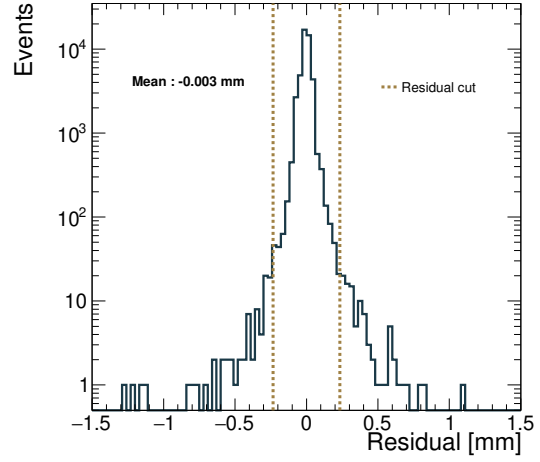


Fig.9. The residual distribution of column 8 in ladder L1.

three categories:

1. Ladder L1 had clusters, and the closest one was close enough to the interpolated point (N_{good}),
2. Ladder L1 had clusters, but the closest one was far from the interpolated point (N_{far}),
3. No cluster was found ($N_{no.hit}$).

The detection efficiency in percentage was defined as Equation 3:

$$\frac{N(L0 \cap L1 \cap L2)}{N(L0 \cap L2)} \times 100\% = \frac{N_{good}}{N_{good} + N_{far} + N_{no.hit}} \times 100\%. \quad (3)$$

The efficiency of ladder L1 was

$$\frac{45498}{45498 + 186 + 123} \times 100 = 99.33\%.$$

The statistical error was estimated using binomial distribution to be $\pm 0.04\%$.

The estimation of the systematic uncertainties was performed. The uncertainties associated with the detection efficiency originated from the determinations of the three cut values, the **edge exclusion**, the **slope cut**, and the **residual cut**. Scanning the cut values gave the variation of each source, and the variation average estimated the uncertainties. The numerical values are summarized in Table 1. Considering the systematic uncertainties, the detection efficiency of ladder L1 was $99.33 \pm 0.04(\text{stat}) \pm 0.06(\text{sys})\%$, excellent enough for the sPHENIX experiment.

Table 1. The sources of the systematic uncertainties affecting the detection efficiency calculation.

Sources	Scan range	Uncertainty (%)
Residual cut	0.164 mm–0.304 mm	0.063
Slope cut	0.0088–0.0112	3×10^{-3}
Edge effect	0 ch–10 ch	4×10^{-4}
Total		0.063

The left-hand side of Figure 10 shows the detection efficiency as a function of the interpolated position. In the beam-spot region indicated by the blue dashed line, the efficiency is independent of the

position, as we expected. In the experiment, the runs with different beam-spot positions were conducted. The efficiency from the run is shown on the right-hand side of Figure 10. The detection efficiency was over 99% at the edge. Therefore, the performance of the INTT ladder was excellent over the column.

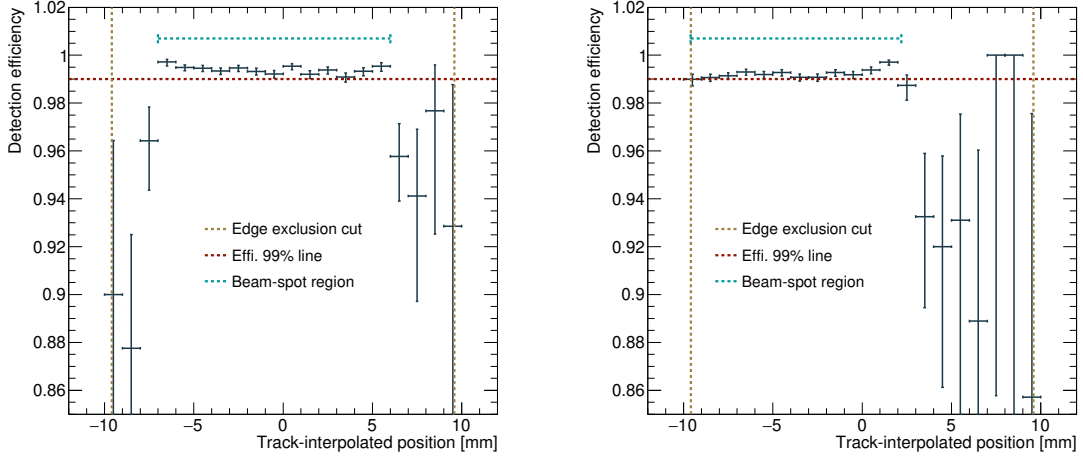


Fig.10. The detection efficiency as a function of the track position. (Left) The beam spot is in the middle. (Right) The beam spot aligns with the edge. The error bars indicate the statistic uncertainties.

§5. Summary

The performance of the INTT mass production ladders was evaluated with the positron beam with the momentum of 1 GeV at the ELPH gamma-ray irradiation room. The experiment was carried out with the two plastic scintillators on the upstream and the downstream as the beam trigger, and various types of measurements were executed.

Eight data collections with different ADC configurations gave the energy deposit curve precisely in the wide range. The curve was successfully made by statistical normalization and well reproduced by the sum of the Landau-Gaussian convolution and the exponential component. The noise contamination to the MIP peak was about 0.3 %, which is evidence of the high detection efficiency of the detector.

The detection efficiency of ladder L1 was estimated by tracking using the upstream and the downstream ladders. After some noise rejections, limitation of the track slope, and the selection of the hit position to the center of the ladder, the detection efficiency of $99.33 \pm 0.04(\text{stat}) \pm 0.06(\text{sys}) \%$ was obtained and uniform over the column-wise region of the silicon sensor.

Acknowledgment

The authors express gratitude to the ELPH accelerator staff for the stable operation of the accelerators for testing the INTT ladders.

References

- [1] C. Aidala *et al.*: Nucl. Instr. Meth. A **755** (2014) 44.
- [2] T. Kondo *et al.*: Trans. Jpn. Inst. Electron. Packag. **15** (2022) E21-007-1.
- [3] A. Suzuki: Master thesis, Nara Women ' s University (2020).
- [4] S. Hancock *et al.*: Phys. Rev. **A28** (1983) 615.

(ELPH Experiment : #2918)

Development of aerogel Cherenkov detectors for use in the EMPHATIC hadron production experiment

Makoto Tabata¹, Karin Okuhata¹, Atsushi Kobayashi¹, Takamichi Yuzawa¹,
and Hideyuki Kawai¹

¹*Department of Physics, Chiba University, Chiba, 263-8522*

We have designed a threshold-type aerogel Cherenkov detector for separating pions and kaons from protons in beams with a momentum of 4–12 GeV/ c and tested its prototype using positron beams. Silica aerogels with refractive indices (n) of 1.003, 1.007, and 1.026 were employed as the Cherenkov radiator. Detected photoelectrons were approximately 44, 11, and 7 for the $n = 1.026$, 1.007, and 1.003 aerogel detectors, where the aerogel thicknesses were 60, 65, and 160 mm, respectively. Experimental results were vital for finalizing the detector's design in the EMPHATIC hadron production measurements at Fermilab, Illinois, USA.

§1. Introduction

To expand charged particle identification capabilities at high momentum ranges (e.g., greater than 5 GeV/ c), employing silica aerogels with low refractive indices as the Cherenkov radiator would be one of the possible solutions but would also be challenging. We are developing a threshold-type aerogel Cherenkov detector for use in the EMPHATIC experiment [1]. This experiment aims to precisely measure hadron productions to reduce uncertainties in neutrino flux predictions. The EMPHATIC uses primary proton beams and their secondary beams delivered at the Fermilab Test Beam Facility (FTBF), Illinois, USA; thus, we need to accurately identify beam particles in front of the production target. Among the beam momenta of 120 GeV/ c , the aerogel detector serves particle identification for pions, kaons, and protons of 4–12 GeV/ c combined with gas Cherenkov detectors, where the maximum gas pressure is limited due to safety reasons. Therefore, developing the aerogel detectors that use high-quality hydrophobic aerogels with different refractive indices (n) is essential for conducting the EMPHATIC experiment.

§2. Results from a test beam experiment

We tested a prototype detector using positron beams with a momentum of 675 MeV/ c at the Research Center for Electron Photon Science, Tohoku University, Japan. As shown in Fig. 1, a light collection box containing a three-sided mirror was viewed by three photomultipliers (PMTs; R6231-100, Hamamatsu Photonics K.K., Japan). Replaceable aerogel containers were attached to the upstream side of the light collection box. The inside walls of the detector were lined with aluminized mylar sheets. We prepared aerogel blocks with $n = 1.003$, 1.007, and 1.026, where the transmission lengths were approximately 14, 13, and 50 mm at a 400-nm wavelength, respectively [2, 3]. Each block size was 45 ×

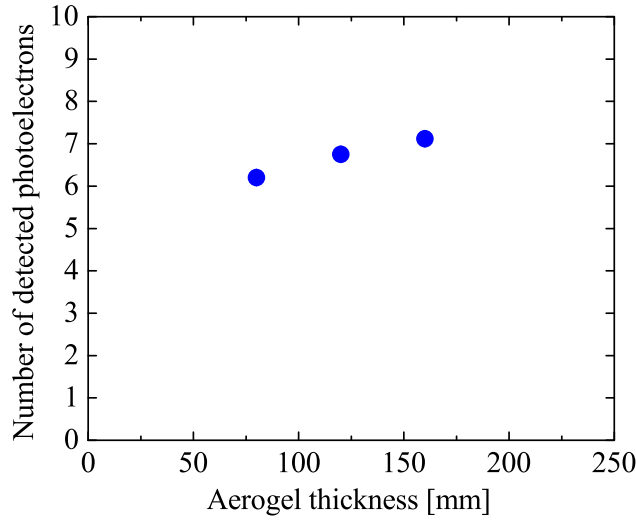


Fig.3. The number of detected photoelectrons versus the aerogel thickness for $n = 1.003$ detector.

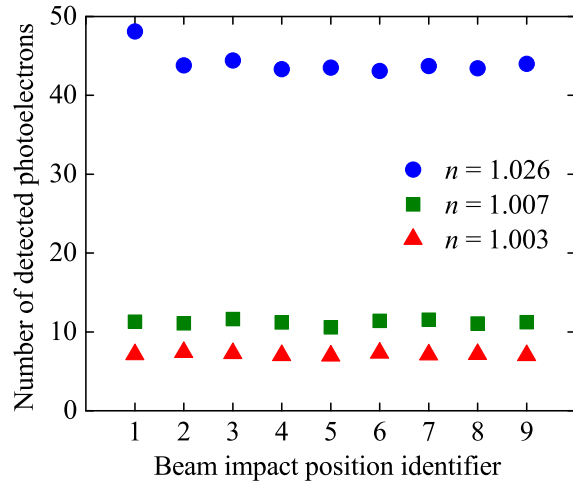


Fig.4. The number of detected photoelectrons versus the beam impact position for positron beams ($\beta \sim 1$).

Figure 5 shows the light yields expected for the actual hadron beams. The light yields for the positron velocity $\beta \sim 1$ were scaled using the actual β for the kaons with momenta of 4, 8, and 12 GeV/ c and pions with 4 GeV/ c . Consequently, we can estimate the light yields for the actual beams as $N_{pe} \sim 31$ (4-GeV/ c kaons), 10 (4-GeV/ c pions), 8 (8-GeV/ c kaons), and 5 (12-GeV/ c kaons), which naively correspond to the detection efficiency of >99.9999%, 99.995%, 99.97%, and 99.3%, respectively.

§3. Summary

We confirmed that the $n = 1.026$ and 1.007 detectors had high detector performances, and the $n = 1.003$ detector was promising in the beam test. Therefore, we believe the detector design tested in this study can be applied to the upcoming EMPHATIC experiment at Fermilab. To increase the $n = 1.003$ detector's performance, we considered increasing the number of PMTs attached from three to

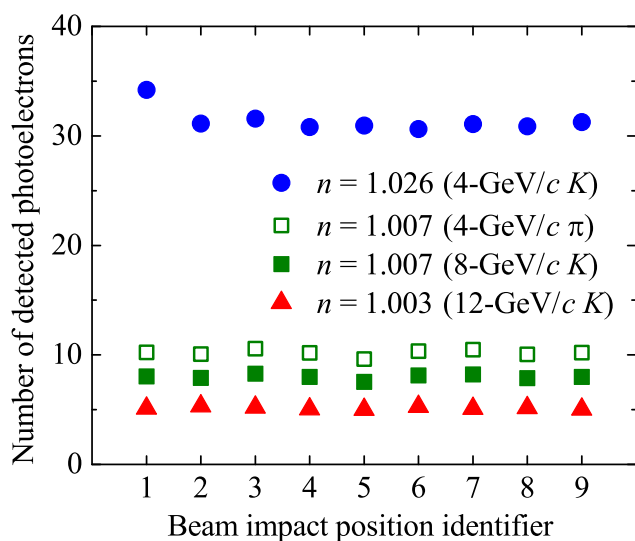


Fig.5. Scaled number of detected photoelectrons versus the beam impact position for 4–12-GeV/c kaon and pion beams.

four. Another solution would be obtained through ongoing studies on further improving the aerogel transparency, enabling the utilization of thick aerogels beyond 160 mm to increase Cherenkov photons emitted.

Acknowledgment

The authors are grateful to the ELPH accelerator staff members for the stable operation of the accelerators while testing the aerogel detector. We are also thankful to Drs. T. Ishikawa, M. Miyabe, and A.O. Tokiyasu for their contributions to the test beam experiment. We thank the members of the EMPHATIC collaboration for fruitful discussions on the aerogel detector design. This study was partially supported by a Grant-in-Aid for Scientific Research (A) (No. 19H00684) from the Japan Society for the Promotion of Science.

References

- [1] T. Akaishi *et al.* (EMPHATIC Collaboration): arXiv:1912.08841.
- [2] M. Tabata *et al.*: Nucl. Instrum. Methods Phys. Res. **A623** (2010) 339.
- [3] M. Tabata *et al.*: Nucl. Instrum. Methods Phys. Res. **A668** (2012) 64.

(ELPH Experiment : #2973)

Commissioning of the twin spectrometers for the ULQ² experiment

C. Legris¹, T. Goke¹, Y. Honda¹, Y. Ishikura¹, M. Kohl², Y. Maeda³, S. Miura¹,
T. Muto¹, T. Suda¹, K. Tsukada⁴, and H. Wauke¹

¹*Research Center for Electron Photon Science, Tohoku University, Sendai, 982-0826*

²*Hampton University, Hampton, Virginia, USA, 23668*

³*Faculty of Engineering, Miyazaki University, Miyazaki, 889-2192*

⁴*Research Center for Nuclear Physics, Osaka University, Osaka, 567-0047*

The determination of the proton charge radius is a hot topic referred as the proton radius puzzle in the nuclear and particle physics communities. At ELPH, the ULQ² (Ultra Low Momentum Transfer) experiment aims at carrying out the most precise measurement of the proton charge radius using the beam with the lowest energy for electron scattering in the world. The measurement is carried out using two identical magnetic spectrometers that focus the electrons scattered on a target in their focal plane, where are placed detectors. This document reports the commissioning of the twin spectrometers for the ULQ² experiment.

§1. The ULQ² experiment

1.1 Proton radius puzzle

Before 2010, measurements of the proton charge radius carried out using electron scattering and atomic hydrogen spectroscopy reported that the proton charge radius was about 0.88 fm [1]. However, in 2010 the proton charge radius was measured for the first time using muonic hydrogen spectroscopy and the determined radius was close to 0.84 fm, 7σ smaller than previous measurements, with a significantly improved accuracy [2]. This result was supported by another measurement of the same group and with the same apparatus in 2013 [3]. Since then, all measurements carried out using electron scattering [4, 5] and atomic hydrogen spectroscopy [6–10] reported a value of either 0.84 or 0.88 fm.

The cause of the discrepancy is still unknown but it was advanced that some experiments were not precise enough [11]. The ULQ² experiment at ELPH aims at solving and understanding the proton charge radius puzzle by measuring the proton charge radius using electron scattering at an extremely low momentum transfer.

1.2 Characteristics of the ULQ² experiment

The ULQ² experiment has three main characteristics: the extremely low Q^2 range, the Rosenbluth separation and the absolute cross-section measurement. The setup of the experiment is displayed in Fig. 1.

Fig. 1. ULQ² beam line.

1.2.1 Extremely low Q^2

The ULQ² beam line currently provides the lowest energy for electron scattering in the world: between 10 and 60 MeV. With this beam line, the ULQ² experiment is carried out with a momentum transfer between 3×10^{-4} and 8×10^{-3} (GeV/c)². Except for the PRad experiment in Jefferson Lab. [5], this is currently the lowest achievable Q^2 worldwide.

1.2.2 Rosenbluth separation

To distinguish the influence of the electric and magnetic form factors, the cross-section is measured at several different angles with a constant Q^2 . It is then possible to extract independently the electric and magnetic form factors under the one-photon exchange approximation. This technique is called Rosenbluth separation and will be applied during the ULQ² experiment.

1.2.3 Absolute cross-section measurement

As the ULQ² experiment uses a plastic (CH₂) target, the electrons are scattered on carbon or hydrogen nuclei. As the momentum of the scattered electrons P_f depends on the mass of the target $M_{H,C}$

$$P_f = \frac{P_i}{1 + \frac{2P_i \sin(\theta/2)^2}{M_{H,C}c}}, \quad (1)$$

with P_i the beam momentum, the momentum of electrons scattered on carbon or hydrogen nuclei differ by several percents. As the momentum acceptance of the spectrometers is about 10 %, it is possible to simultaneously observe and distinguish the electrons scattered on carbon or hydrogen nuclei. The absolute cross-section of the electron-proton scattering can then be expressed as a function of the cross-section of the electron-carbon scattering, which has been widely studied [12–15], the number of electrons on the detectors $N_{e-H,C}$ and the number of target nuclei $N_{H,C}$ in the plastic target

$$\left(\frac{d\sigma}{d\Omega}\right)_H = \frac{N_{e-H}/N_{e-C}}{N_H/N_C} \left(\frac{d\sigma}{d\Omega}\right)_C. \quad (2)$$

Measuring the absolute cross-section of the electron-proton scattering significantly increases the accuracy of the measurement as the precise determination of the beam current and the acceptance of the spectrometers are not required.

1.3 Description of the ULQ² spectrometers

The ULQ² experiment uses two high-resolution spectrometers built with the same design by the TOKIN company. The first spectrometer was installed in 2019 and has been partially commissioned in November 2020 [16] while the second one was installed in August 2021. The first spectrometer measures the ratio of the yield of the electron-carbon and the electron-hydrogen scatterings with different angles. As the carbon-hydrogen nuclei ratio in the target is known to change due to beam irradiation, the second spectrometer acts as a luminosity monitor: by keeping the second spectrometer in the same position, it monitors the status of the CH₂ target with fixed angle and energy. The hydrogen and carbon peaks have to be resolved for the lowest momentum transfer: $Q^2 = 3 \times 10^{-4} \text{ (GeV/c)}^2$, so the main requirement for the ULQ² spectrometers is to have a momentum resolution better than 10^{-3} .

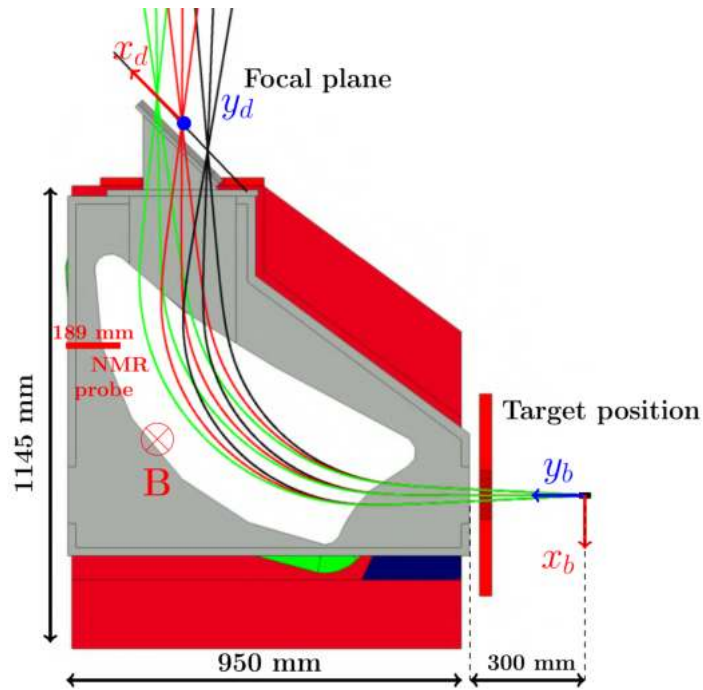


Fig. 2. Cross-section view of the ULQ² spectrometers.

Spectrometers are dipole magnets used to measure the momentum and the scattering angle of the electrons scattered off by the target (see Fig. 2). The basic characteristics of the spectrometers are described in Table 1. These spectrometers are designed to focus scattered electrons in their focal plane, where are located detectors. Since no tracking technique can be applied due to the extremely low momentum of scattered electrons, they were carefully designed so that the momentum and the scattering angle of scattered electrons are obtained with the required accuracy only from their 2D position on the detectors.

Weight	3650 kg
Height	1145 mm
Length	950 mm
Bending angle	90°
Curvature radius	500 mm
Distance from the target	300 mm
Accessible scattering angles	30°-150°
Accuracy of the spectrometer angle	0.1 mrad
Angular acceptance	~ 10 mSr
Momentum acceptance	~ 10%

Table 1. Characteristics of the ULQ² spectrometers.

The (x_d, y_d) position on the detectors is related to the initial parameters such as the beam position on the target (x_b, y_b) or the momentum and angle θ of the scattered electrons by a Taylor expansion (α, β, γ and ν are here integers) [17]:

$$x_d = \sum_{\alpha\beta\gamma\nu} (x_d | x_b^\alpha y_b^\beta \Delta\theta^\gamma \delta^\nu) x_b^\alpha y_b^\beta \Delta\theta^\gamma \delta^\nu \quad (3)$$

$$y_d = \sum_{\alpha\beta\gamma\nu} (y_d | x_b^\alpha y_b^\beta \Delta\theta^\gamma \delta^\nu) x_b^\alpha y_b^\beta \Delta\theta^\gamma \delta^\nu. \quad (4)$$

Mainly, it can be noted that the y_d position is proportional to the angle of the scattered electron with $(y_d | \Delta\theta)$ the angular dispersion ($\Delta\theta = \theta - \theta_{SP}$ and θ_{SP} is the spectrometer angle). The x_d position is proportional to δ with $(x_d | \delta)$ the momentum dispersion. The variation of momentum from the central orbit is described by

$$\delta = \frac{p_s - p_c}{p_c} = \frac{B_s - B_c}{B_c}, \quad (5)$$

with p_s the momentum of the scattered electron proportional to B_s and B_c the magnetic field of the spectrometer proportional to p_c . As the momentum acceptance of the spectrometers is about 10 %, δ can vary between -0.05 and 0.05. A typical spectrum obtained with a CH₂ target is displayed in Fig. 3.

1.4 Detectors

Due to the strong multiple scattering at low energy, the number and thickness of the detectors have to be reduced as small as possible. The detectors placed in the focal plane of the spectrometers are Single Sided Silicon Strip Detectors (SSSSDs), jointly developed with the J-PARC/g-2 muon EDM collaboration [18]. Each detector can measure the position along one direction so on top of each spectrometer, two SSSSDs measuring respectively the x_d and y_d positions are used (see Fig. 2). Each detector is composed of 2×512 channels with a width of 0.19 mm and a thickness of 0.32 mm, covering a surface of 98.77×98.77 mm². Signals are digitized onboard and transmitted to PC using network.

1.5 Geant4 simulation

In addition to the ULQ² experimental setup, a Geant4 Monte-Carlo simulation is used to study the performance of the spectrometers. The magnetic field used in the simulation is calculated with the

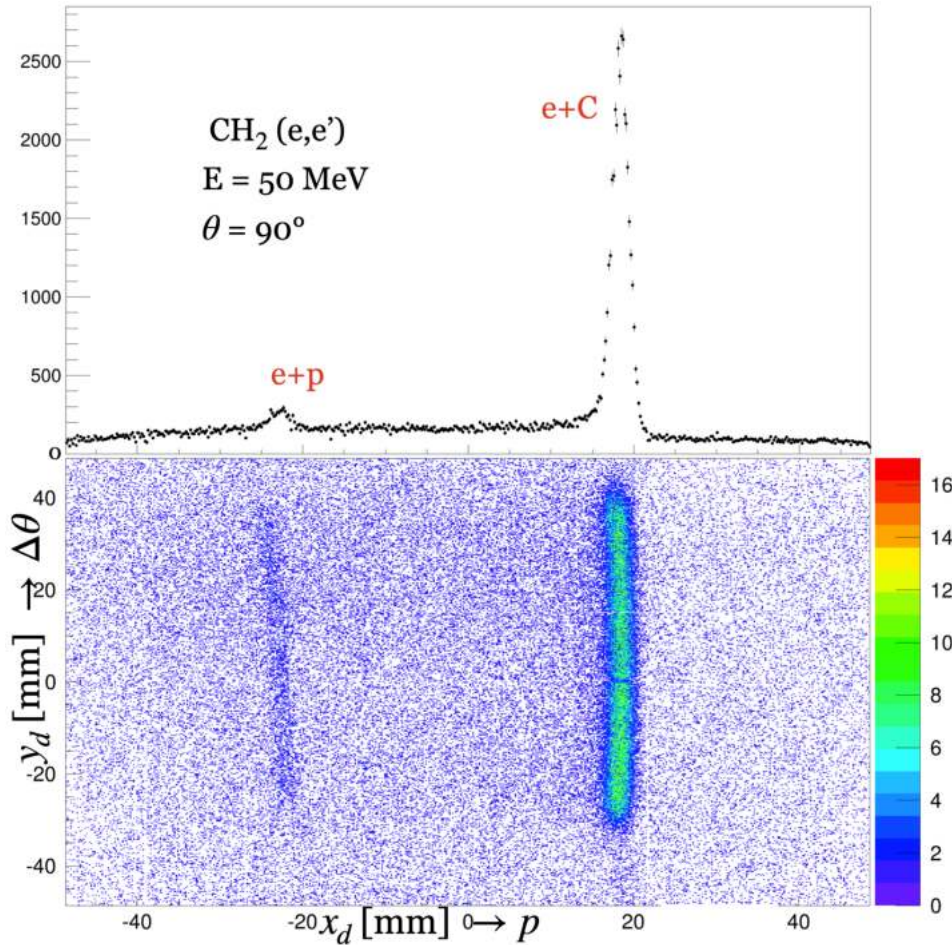


Fig. 3. (Down) 2D spectrum obtained during the commissioning experiment with the second spectrometer using a CH_2 target and the $20 \times 20 \text{ mm}^2$ squared-hole collimator (see subsection 2.2). (Up) Projection along the x_d axis.

TOSCA analysis package and the Opera 3D software [19]. In this simulation, there is also:

- a $130\text{-}\mu\text{m}$ -thick CH_2 target,
- a collimator supporter and a collimator that are placed in the same condition as during the commissioning experiment,
- detectors that are placed in the focal plane of the spectrometers.

Electrons are generated in the target with Gaussian distributions along x_b (vertical) and y_b (horizontal) axes. The energy distribution also follows a Gaussian distribution. The beam position and beam energy spread that were used were the ones measured in experiment: $\sigma_{x_b, y_b} \sim 1 \text{ mm}$ and $\sigma_E \sim 10^{-3}$.

§2. Commissioning results

2.1 Experimental conditions

The commissioning of the twin spectrometers aimed at determining the transfer matrix elements of the spectrometers and confirming that they are consistent with designed values and simulations [20]. The commissioning was carried out with the spectrometers set at 90° and using a $130\text{-}\mu\text{m}$ -thick CH_2 target. The beam energy was fixed during the whole experiment at 50 MeV and the spectrometers

were placed at 90° . As the current of the spectrometers is proportional to the magnetic field of the spectrometers, changing the current of the spectrometers allows to vary δ (Eq. (5)) in order to determine the momentum dispersion. Data was recorded for 30 minutes with nine different currents applied to the spectrometers from 186 A to 202 A. The magnetic field of each spectrometer was monitored by NMR probes placed at the back of the spectrometers.

2.2 Squared-hole collimators

5-mm thick collimators with $20 \times 20 \text{ mm}^2$ holes were placed 290 mm away from the target at the entrance of the spectrometers. The shape of the collimators defined the horizontal and vertical angular acceptances of the spectrometers: with the spectrometers placed at 90° , $(\Delta\theta, \Delta\phi) \in [-33.9, 33.9]$ mrad. The 2D spectrum obtained with the second spectrometer and a 188-A current is displayed in Fig. 3.

2.2.1 Momentum dispersion

The carbon peak x_d position was determined for each current applied to the spectrometer (9 different currents from 186 A to 202 A). Only the electrons that hit the center of the SSSSDs were used in this analysis ($y_d \in [-9.69, 9.69]$ mm in Fig. 3) because the scattering angle has an impact on x_d (see subsection 2.3.1). The following fitting between x_d and B_c was then conducted to determine B_s , $(x|\delta)$ and $(x|\delta^2)$:

$$x_d = x_0 + (x_d|\delta) \frac{(B_s - B_c)}{B_c} + (x_d|\delta^2) \frac{(B_s - B_c)^2}{B_c}. \quad (6)$$

x_0 is a fixed constant term that corrected the horizontal misalignment of the detectors on top of the spectrometers. It is equal to 4.9 mm and -1.8 mm for the first and second spectrometers respectively. The result of the fitting for both spectrometers can be seen in Fig. 4. It was noticed that the beam energy as well as the beam vertical position on the target were fluctuating during the measurements causing variations of x_d of several tens of μm so the accuracy of the peak position was set to $\pm 100 \mu\text{m}$.

Geant4 simulations of the ULQ2 spectrometers showed that the angle of the detectors had a strong impact on the momentum dispersion. The momentum dispersion difference between both spectrometers was likely caused by slight misplacements (of the order of a few hundreds of μm) of the detectors in the focal plane of the spectrometers.

2.2.2 Momentum resolution

The measured momentum resolution σ'_p was calculated from experimental data as follows, with σ_{x_d} the standard deviation of the carbon scattering peak:

$$\sigma'_p = \frac{\sigma_{x_d}}{\frac{\partial x_d}{\partial \delta}} = \frac{\sigma_{x_d}}{(x_d|\delta) + 2\delta(x_d|\delta^2)}. \quad (7)$$

This measured momentum resolution had to be corrected as it included the vertical beam position spread ($\sigma_{x_b} \sim 0.66 \text{ mm}$ and $(x_d|x_b) = 0.510 \pm 0.005 \text{ mm/mm}$) as well as the beam energy spread ($\sigma_E \sim 8.9 \times 10^{-4}$). The vertical position spread and the beam energy spread were measured by placing a screen respectively in the target position or in the second dispersive plane of the beam line. If we suppose that

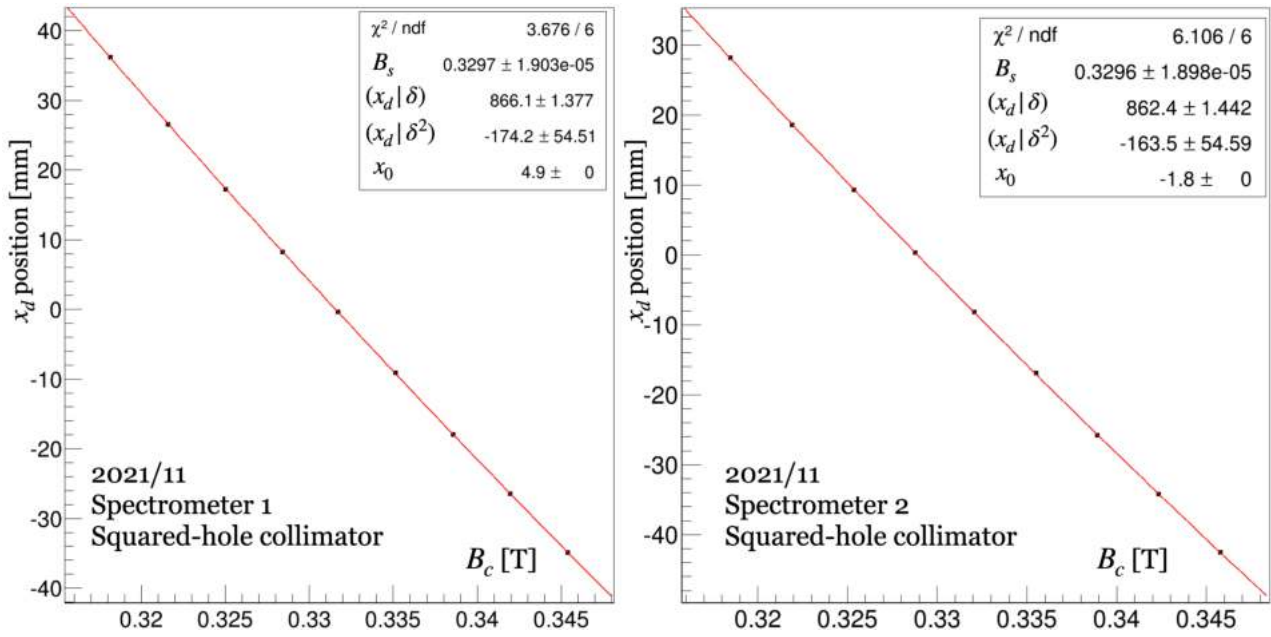


Fig. 4. Relation between x_d and B_c for the first (left) and second (right) spectrometers.

the beam energy spread and the beam vertical spread were completely independent ($(x_d | x_b \delta) \Delta x_b \Delta \delta \ll 1$), the intrinsic momentum resolution σ_p is defined as

$$\sigma_p = \sqrt{\sigma_p'^2 - \left(\frac{(x_d | x_b) \sigma_{xb}}{(x_d | \delta) + 2\delta(x_d | \delta^2)} \right)^2}. \quad (8)$$

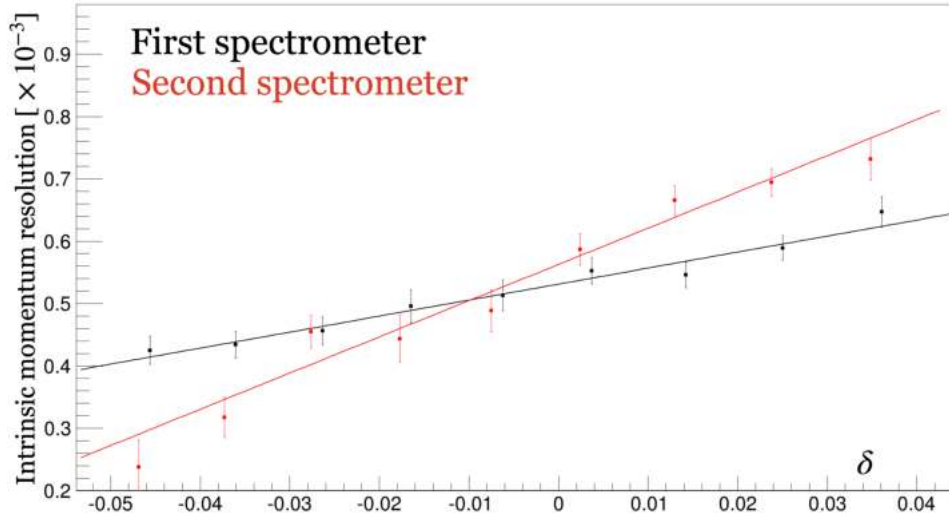


Fig. 5. Intrinsic momentum resolution for both spectrometers.

The intrinsic momentum resolution with respect to δ is displayed in Fig. 5. When $\sigma = 0$, the intrinsic momentum resolution of the detectors was similar for both spectrometers (about 5.5×10^{-4}). As the momentum resolution was smaller than 10^{-3} for any value of δ , the intrinsic momentum resolution fulfilled the main requirement of the spectrometers.

2.3 Sieve slit collimators

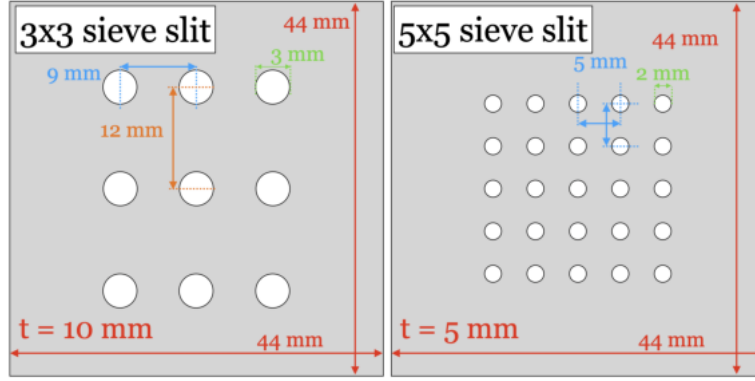


Fig. 6. Sieve slits used during the commissioning experiment.

To study the influence of the scattering angle on the (x_d, y_d) -position, sieve slits were placed in front of the collimators (see Fig. 6). The 3 x 3 sieve slit was used for the first spectrometer. It was placed 285 mm from the target, its thickness was 10 mm, its hole diameter was 3 mm, the accepted horizontal angles $\Delta\theta$ were $\{-30.5, 0, 30.5\}$ mrad and the accepted vertical angles $\Delta\phi$ were $\{-40.6, 0, 40.6\}$ mrad, respectively. The 5 x 5 sieve slit was used for the second spectrometer. It was placed 290 mm from the target, its thickness was 5 mm, its hole diameter was 2 mm, the accepted horizontal and vertical angles were $\{-33.9, -16.9, 0, 16.9, 33.9\}$ mrad. Typical 2D spectra obtained with the sieve slits collimators are displayed in Fig. 7.

2.3.1 Impact of the scattering angle on x_d

For any given spectrometer current and for each peak position, the x_d position was fitted as a function of $\Delta\theta$ as follows:

$$x_d = X + (x_d|\Delta\theta^2)[\Delta\theta - \theta_0]^2. \quad (9)$$

θ_0 was added to compensate a shift along the y_d axis. If θ_0 is equal to 0, X corresponds to x_d in Eq. (6). As θ has an influence on the momentum of the scattered electron, a small correction term was added so that all the peaks had the same δ . The correction term is

$$dx_d(\theta) = \frac{p_f(50 \text{ MeV}, 90^\circ) - p_f(50 \text{ MeV}, \theta)}{50 [\text{MeV}/c]} (x_d|\delta). \quad (10)$$

This term is negative for forward angles, positive for backward angles and accounts for about 0.1 mm at ± 33.9 mrad.

The values of $(x_d|\Delta\theta^2)$ and θ_0 that were obtained from fittings are displayed in Fig. 8. $(x_d|\Delta\theta^2)$ and θ_0 can safely be considered constant and only had an impact on x for large y values: $(x_d|\Delta\theta^2) \times (34 \text{ mrad})^2 \sim 0.5 \text{ mm}$.

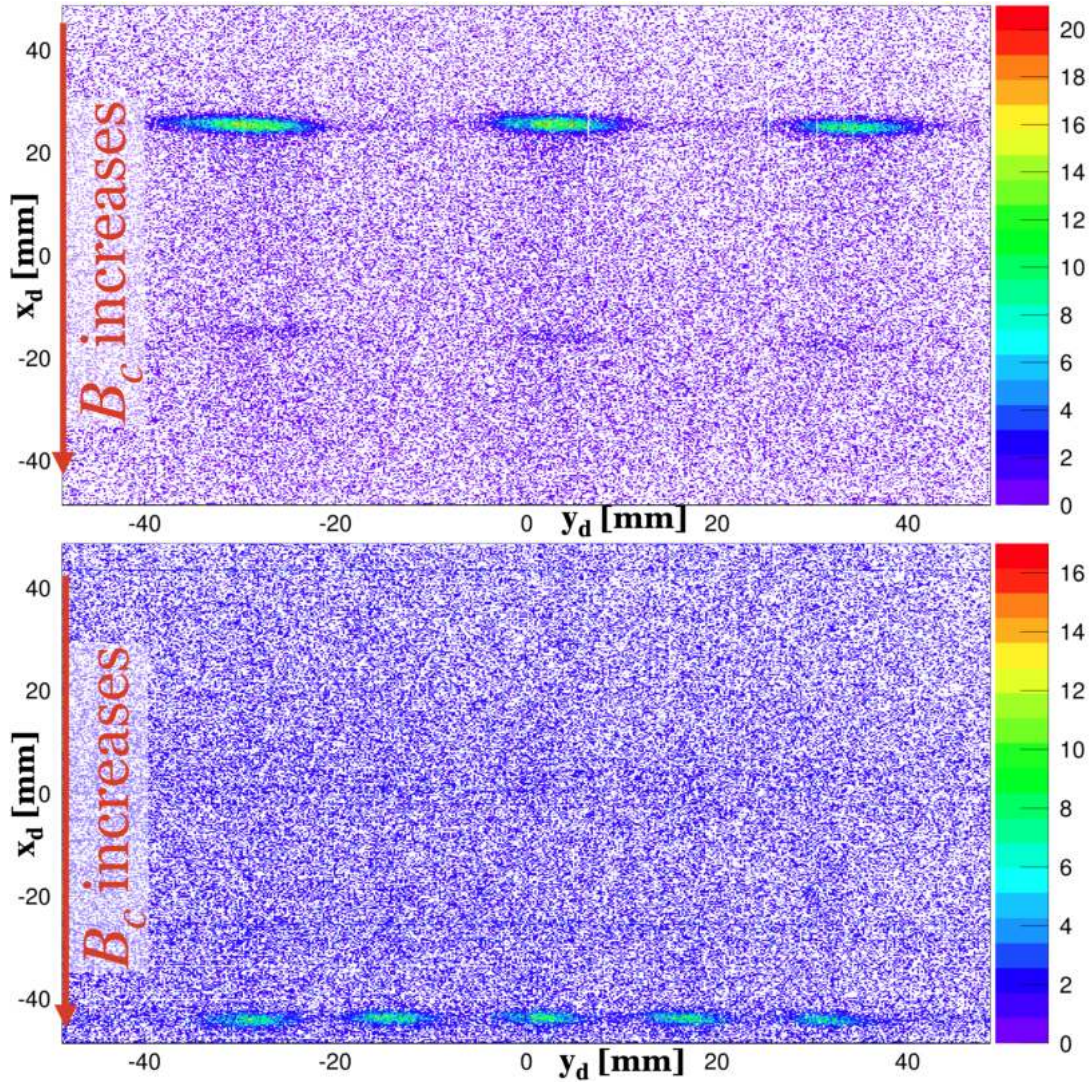


Fig. 7. 2D hitmap obtained with the first spectrometer using the 3 x 3 sieve slit when the current was set to 188 A (up) and with the second spectrometer using the 5 x 5 sieve slit when the current was set to 202 A (down). Forward and backward angles respectively correspond to negative and positive y_d .

2.3.2 Impact of the scattering angle on y_d

For any given spectrometer current and for each peak position, the y_d position was determined and fitted as a function of $\Delta\theta$ as follows:

$$y_d = (y_d|\Delta\theta)' \Delta\theta, \quad (11)$$

where $(y_d|\Delta\theta)'$ corresponds to the angular dispersion of the spectrometers. It can be noted in Fig. 7 that the angular dispersion depends on δ . For that reason, the δ dependence of the angular dispersion was studied using a linear fitting, with $(y_d|\Delta\theta)$ and $(y_d|\delta\Delta\theta)$ respectively the first and second order terms of the angular dispersion:

$$(y_d|\Delta\theta)' = (y_d|\Delta\theta) + \delta(y_d|\delta\Delta\theta) \quad (12)$$

It can be noticed in Fig. 9 that even though the angle of the detectors on top of the spectrometers

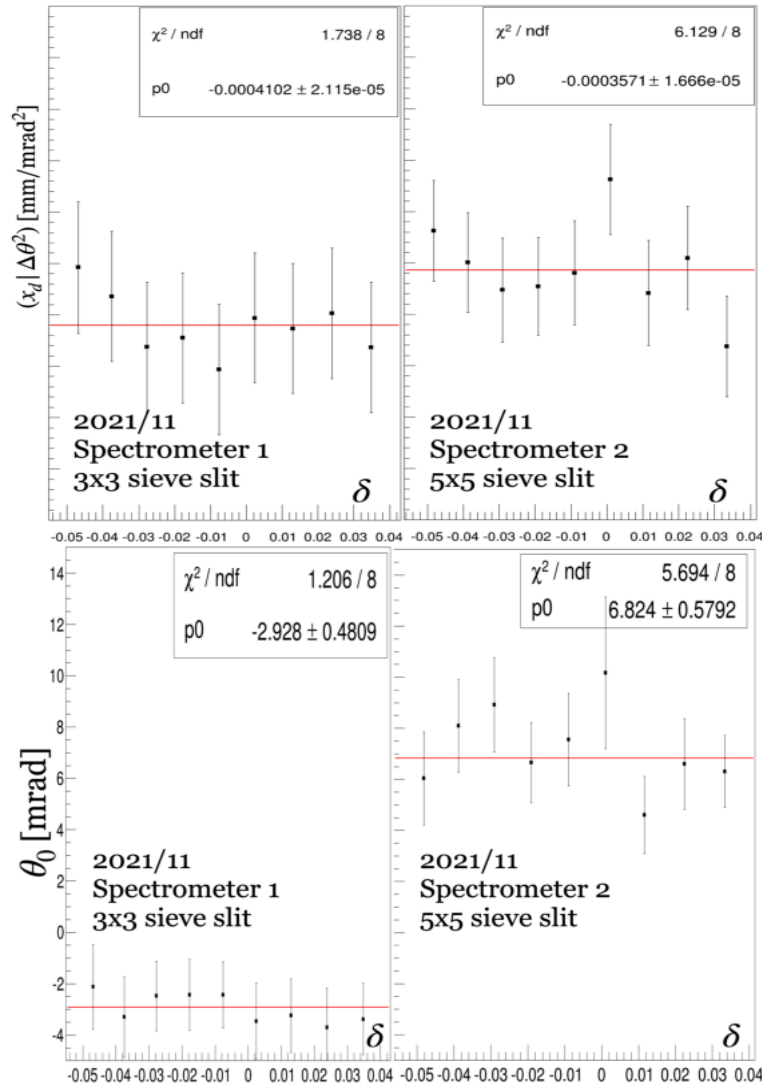


Fig. 8. $(x_d | \Delta\theta^2)$ and δ_0 for the first and second spectrometers.

was different, the terms of the angular dispersion were consistent for both spectrometers.

However, it can be seen in Fig. 10 that the angular dispersions measured during the commissioning experiment disagree with the angular dispersion obtained from the Geant4 simulation by about 4%.

This discrepancy is very likely caused by a difference between the magnetic field measured by TOKIN and the magnetic field calculated using Opera 3D at the exit of the spectrometer (see Fig. 11). The magnetic field is negative and the integral of the difference between the magnetic fields is positive so the calculated magnetic field is weaker than the actual one. It can then reasonably be assumed that the angular dispersion in the simulation is underestimated, which is consistent with the results of the commissioning experiment.

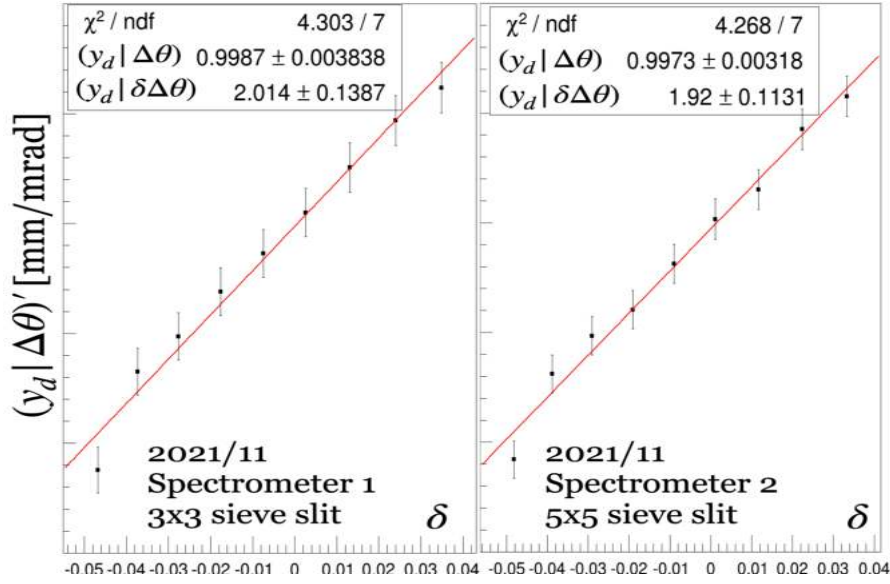


Fig. 9. Relation between $(y_d|\Delta\theta)'$ and δ for the first (left) and second (right) spectrometers.

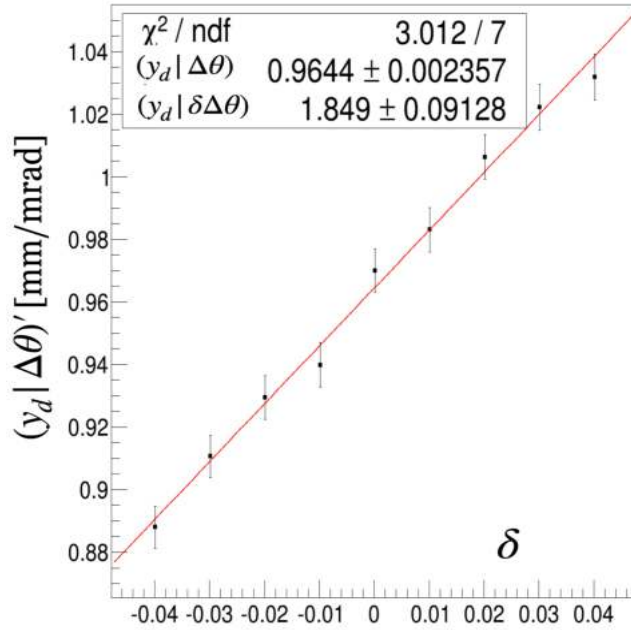


Fig. 10. Relation between $(y_d|\Delta\theta)'$ and δ from the Geant4 simulation.

§3. Conclusion

Using the data obtained during the commissioning experiments, the relation between the (x_d, y_d) -position and the initial parameters $(\delta, \Delta\theta, x_b, y_b)$ was determined:

$$\begin{cases} x_d = x_0 + (x_d|\delta)\delta + (x_d|\delta^2)\delta^2 + (x_d|\Delta\theta^2)[\Delta\theta - \theta_0]^2 + (x_d|x_b)x_b \\ y_d = [(y_d|\Delta\theta) + \delta(y_d|\delta\Delta\theta)]\Delta\theta + (y_d|y_b)y_b \end{cases} \quad (13)$$

The results are summarized in Table 2.

The following results should be emphasised:

- the difference between the momentum dispersions of each spectrometer can be accounted for a

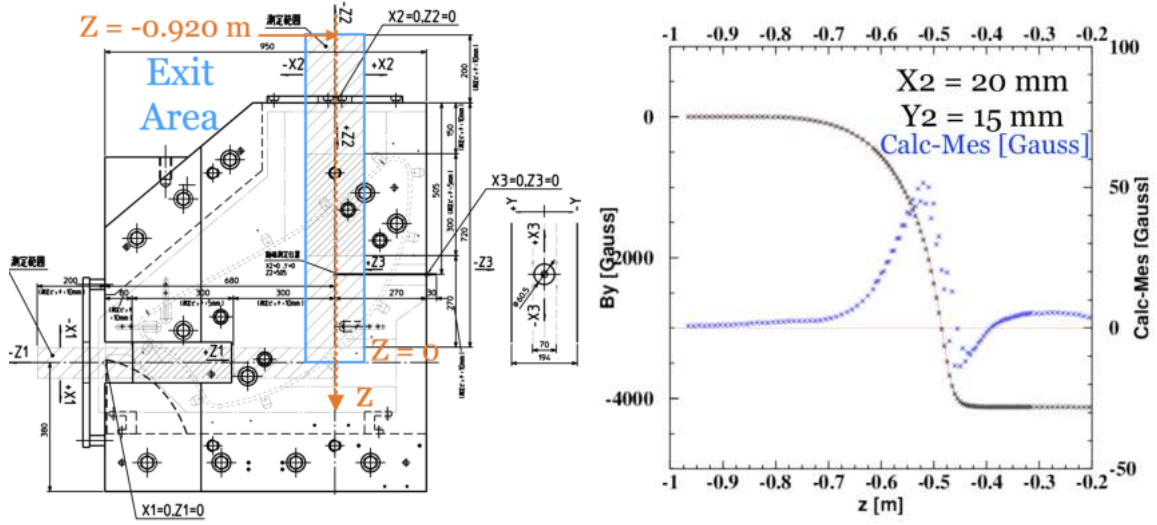


Fig. 11. (Left) Exit area of the spectrometer. (Right) Difference between the measured and calculated magnetic field in this area.

Parameters	Spectrometer 1	Spectrometer 2
x_0 [mm]	4.9	-1.8
$(x_d \delta)$ [mm]	866.1(7)	862.4(7)
$(x_d \delta^2)$ [mm]	-174(26)	-164(26)
$(x_d \Delta\theta^2)$ [10^{-4} mm/mrad ²]	-4.1(2)	-3.6(2)
θ_0 [mrad]	-2.9(5)	6.8(6)
$(y_d \Delta\theta)$ [mm/mrad]	0.999(4)	0.997(3)
$(y_d \delta\Delta\theta)$ [mm/mrad]	2.01(14)	1.92(11)
σ_p ($\delta=0$) [10^{-3}]	5.28(7)	5.71(10)

Table 2. Summary table.

difference in the detector angle,

- both spectrometers fulfill the requirement on the intrinsic momentum resolution: it was found smaller than 10^{-3} ,
- the angular dispersions measured in the focal plane of the twin spectrometers are consistent with each other but differ of about 4 % with the Geant4 simulation.

We conclude that the initial conditions ($\Delta\theta$, δ , x_b , y_b) of electrons hitting the detectors can be determined from the (x_d, y_d) positions on the detectors with the matrix parameters that were determined during the commissioning experiments. Experimental results are consistent with simulations, except for $(y_d|\Delta\theta)$. This discrepancy is very likely to be caused by differences between the calculated and measured magnetic field at the exit of the spectrometers.

Acknowledgment

This work was supported in part by JSPS KAKENHI Grants Nos. 16H06340, 18K13553, 20H05635 and the Graduate Program on Physics for the Universe (GP-PU), Tohoku University.

References

- [1] P. J. Mohr *et al.*, Rev. Mod. Phys. **84** (2012) 8-18
- [2] R. Pohl *et al.*, Nature **466** (2010) 213.
- [3] A. Antognini *et al.*, Science **339** (2013) 417.
- [4] J. C. Bernauer *et al.*, Phys. Rev. C **90** (2014) 015206.
- [5] W. Xiong *et al.*, Nature **575** (2019) 147.
- [6] A. Beyer *et al.*, Science **358** (2017) 79.
- [7] H. Fleurbaey *et al.*, Phys. Rev. Lett. **120** (2018) 183001.
- [8] N. Bezginov *et al.*, Science **365** (2019) 1007.
- [9] A. Grinin *et al.*, Science **370** (2020) 1061.
- [10] A. D. Brandt *et al.*, Phys. Rev. Lett. **128** (2022) 023001.
- [11] I. Sick, Atoms **6** (2018) 2.
- [12] W. L. Faissler *et al.*, Phys. Rev. Lett. **19** (1967) 1202.
- [13] W. Reuter *et al.*, Phys. Rev. C **26** (1982) 806.
- [14] W. Ruckstuhl *et al.*, Nucl. Phys. A **430** (1984) 685.
- [15] E. Offermann *et al.*, Phys. Rev. C **44** (1991) 1096-1117.
- [16] D. Taki, Master's thesis, Tohoku University (2020).
- [17] K. L. Brown, SLAC Report 75 (1971)
- [18] T. Aoyagi *et al.*, JINST **15** (2020) P04027.
- [19] OPERA 3D (TOSCA) <https://www.3ds.com/products-services/simulia/products/opera/>
- [20] Y. Honda *et al.*, ELPH Annual Report, Tohoku University (2019) 75.

(ELPH Experiment : #2947)

Mass production of Sc-47 by photonuclear reaction for nuclear medicine application

Hidetoshi KIKUNAGA¹, Atsushi TOYOSHIMA², Hayato IKEDA^{1,3},
and Yuki HONDA¹

¹Research Center for Electron Photon Science, Tohoku University, Sendai, 982-0826

²Institute for Radiation Sciences, Osaka University, Toyonaka, 560-0043

³Cyclotron and Radioisotope Center, Tohoku University, Sendai, 980-8578

Scandium-46 and Scandium-47 are nuclides useful or expected to be useful in various fields such as radiotherapy and basic research. It is important to produce these nuclides separately depending on the application. In this work, the radioactivity ratios of ⁴⁶Sc and ⁴⁷Sc produced by photonuclear reactions from ^{nat}Ti and ⁴⁸Ti targets have been determined. ^{nat}TiO₂ and ⁴⁸TiO₂ were enclosed in a quartz tube for bremsstrahlung radiation. The irradiations were performed using the electron linear accelerator at Tohoku University. The accelerator was operated at an electron energy of 20-50 MeV. The TiO₂ targets were placed in close contact with the back of a Ta converter and cooled with running tap water during the 10-30 min irradiation. After irradiation, the targets were examined by gamma spectrometry using a high-purity Ge semiconductor detector.

§1. Introduction

The scandium isotope with mass number 47 (⁴⁷Sc) has a moderate half-life ($T_{1/2}$: 3.35 d), maximum energy of β radiation ($E_{\beta} = 440$ keV (68%) and 600 keV (32%)), and γ -ray emission properties suitable for SPECT imaging ($E_{\gamma} = 159$ keV (68%)). Therefore, it is expected to be used for theranostics. Our research group has established a production method for Sc isotopes, including chemical purification, by photonuclear reaction using Ti isotopes of less than 1 g. In this study, production tests were conducted with an increased target amount of 5-10 g to provide a large amount of ⁴⁷Sc for basic research in nuclear medicine. In addition, ^{nat}CaO and ^{nat}ZnO irradiation tests using the same amount of target elements were also performed to compare the difference in damage caused by different target elements.

§2. Experimental

The irradiation samples were enclosed in quartz tubes of 16 mm or 21 mm inner diameter, in which ^{nat}TiO₂ powder was pressed with a Teflon rod or molded by a press machine. Irradiation was performed using a high-intensity electron linear accelerator at the Research Center for Electron Photon Science, Tohoku University. An electron beam of about 130 μ A accelerated to 30 MeV was converted to bremsstrahlung by a 3 mm thick Ta-based water-cooled converter, and each sample was irradiated for

2-6 hours with water cooling.

After irradiation, the samples were chemically separated by scaling up the procedure used for separations of 1 g or less. After dissolving the samples in hydrofluoric acid, a fraction was separated and the amount of ^{47}Sc was determined by γ -spectrometry using a high-purity Ge semiconductor detector. The remaining sample was purified by cation exchange without any carrier, and the applicability of the previous procedure to a few g scale was examined.

Samples of ^{nat}CaO and ^{nat}ZnO were prepared and irradiated in the same manner, and after visual confirmation, some of them were dissolved in HCl and subjected to γ -spectrometry.

§3. Results

A photograph of the enclosed specimen after irradiation is shown in Fig. 1(a), and $^{nat}\text{TiO}_2$ transferred to the crucible is shown in Fig. 1(b). Although the $^{nat}\text{TiO}_2$ was uniformly filled before irradiation, the area most strongly irradiated by the beam decreased in volume after irradiation and became darker. This area was much harder than the white $^{nat}\text{TiO}_2$ and was not easily dissolved by hydrofluoric acid. When heated to 850-900C in air using an electric furnace, it turned white and could be dissolved by hydrofluoric acid. Probably, a part of $^{nat}\text{TiO}_2$ was reduced by irradiation and became an insoluble compound. Such insoluble substances do not occur in ^{nat}CaO and ^{nat}ZnO , however, their properties changed before and after irradiation, and it is necessary to change the chemical purification procedure.

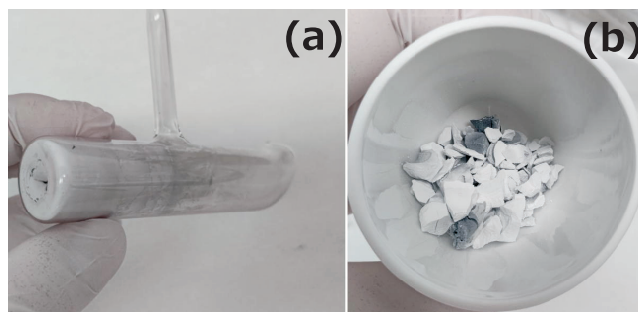


Fig.1. Enclosed sample after irradiation(a); internal $^{nat}\text{TiO}_2$ (b)

II. Status Report

III. List of Publication

IV. Members of Committees

V. Approved Experiments

ELPH Annual Report 2021

(April 2021-March 2022) March 2023

ONLINE ISSN 2435-9165

Published by

Research Center for Electron-Photon Science (ELPH), Tohoku University

1-2-1 Mikamine, Taihaku, Sendai, Miyagi 982-0826, Japan

Phone: +81-22-743-3411

FAX: +81-22-743-3402

Email: koho@lms.tohoku.ac.jp

Homepage: <https://www.lms.tohoku.ac.jp/>

Copyright © 2023 ELPH

All rights reserved

2023 年（令和 5 年）3 月 31 日 発行

発行者 国立大学法人東北大学電子光理学研究センター
センター長 須田 利美

〒982-0826 宮城県仙台市太白区三神峯 1-2-1

電話： 022-743-3411

FAX： 022-743-3402

Email： koho@lms.tohoku.ac.jp

ホームページ： <https://www.lms.tohoku.ac.jp/>

